NOVA SCHOOL OF SCIENCE & TECHNOLOGY

DEPARTMENT OF PHYSICS

DIOGO BENTO NEVES

BSc in Engineering Physics

RADIOACTIVE MATERIAL, FLUORINE AND RARE-EARTH ELEMENT QUANTIFICATION IN PHOSPHOGYPSUM USING NUCLEAR ANALYTICAL TECHNIQUES

MASTER IN ENGINEERING PHYSICS

NOVA University Lisbon
November, 2024

NOVA SCHOOL OF SCIENCE & TECHNOLOGY

DEPARTMENT OF PHYSICS

RADIOACTIVE MATERIAL, FLUORINE AND RARE-EARTH ELEMENT QUANTIFICATION IN PHOSPHOGYPSUM USING NUCLEAR ANALYTICAL TECHNIQUES

DIOGO BENTO NEVES

BSc in Engineering Physics

Adviser: Dr. João Duarte Neves Cruz
Associate Professor, NOVA University Lisbon

Co-adviser: Dr. Sofia Verónica Trindade Barbosa
Assistant Professor, NOVA University Lisbon

Examination Committee

Chair: Dr. Paulo António Martins Ferreira Ribeiro
Associate Professor, NOVA University Lisbon

Rapporteur: Dr. Daniel Galaviz Redondo
Assistant Professor, University of Lisbon

Adviser: Dr. João Duarte Neves Cruz
Associate Professor, NOVA University Lisbon

MASTER IN ENGINEERING PHYSICS

NOVA University Lisbon
November, 2024

Radioactive Material, Fluorine and Rare-Earth Element Quantification in Phosphogypsum Using Nuclear Analytical Techniques

This document was created with the (pdf/Xe/Lua)LaTeX processor and the NOVAthesis template (v7.1.18) [1].

Acknowledgements

I begin by thanking my adviser, Professor João Cruz, for his unwavering support in the last few months and for everything he taught me about nuclear physics, both in class and throughout the course of this work. I also thank Professor Sofia Barbosa, for generously providing valuable material, that helped me get acquainted with this work's main objective, as well as for her guidance in the final chapter of this dissertation, on a topic I was unfamiliar with.

I would like to extend my gratitude to everyone at NOVA FCT who played a significant role in shaping my path over the past five years. I also appreciate the assistance from everyone who contributed to my work at CTN-IST.

Finally, and most importantly, I want to thank my girlfriend, family, and friends for their constant support and for always believing in my ability to achieve my goals.

”

“The most important thing about a journey is to arrive at its end, but the real pleasure lies in the interval between departure and arrival.”

— Paul Theroux

Abstract

Phosphogypsum (PG) is the main by-product of wet processing of phosphate rock, to generate phosphoric acid. Estimates point to a yearly production of 100 to 280 million tonnes, with worldwide stockpiles amounting to close to 6 billion tonnes. With an increasing demand for gypsum based materials for industrial and agricultural applications and the predictable gypsum shortage in the coming years, PG can be considered a valuable replacement.

High concentrations of uranium-238 and thorium-232 decay series radionuclides and fluorine limit the possibility of use of PG, given the negative effects these contaminants can have on human health and the environment. The aim of the experiments, as part of the Phosphogypsum Processing to Critical Materials (PG2CRM) project, was to chemically characterize PG samples to help develop purification techniques and enable its use as an inexpensive raw material.

Seventeen samples, from Germany and France, were analysed using Particle Induced Gamma-ray Emission (PIGE), Particle Induced X-ray Emission (PIXE) and Elastic Backscattering Spectrometry (EBS). The use of these techniques allowed for complete sample characterization, with emphasis on fluorine, for being extremely difficult to accurately quantify using other methods, and rare-earth elements (REE), given the high economical value of these elements should they be extracted from PG.

Results showed high concentrations of calcium (26 wt.%-29 wt.%) and sulphur (19.4 wt.%-23.8 wt.%). Sodium, aluminium, silicon, titanium, iron and strontium were present in low concentrations (up to 2 wt.%) throughout the samples. A few outlier values were encountered for elements like phosphorus and chlorine, which show increased concentration in some samples. These were attributed to decontamination treatments previously applied to the samples. Fluorine concentrations ranged from 0.003 wt.% to 0.691 wt.%, with even the lowest values surpassing the concentration limits imposed for water contamination and for use in the gypsum industry. REE detection was not significant, with only small amounts of cerium and gadolinium observed.

A radiological risk assessment was performed, showing that most samples had relatively low radionuclide concentrations, with an average Radium equivalent activity of 265.04 Bq/kg and average values of 0.89, 0.72 and 1.29 for gamma, external and internal hazard indexes, respectively. The Annual Effective Dose (AED) for indoor and outdoor scenarios were below the 1 mSv/y limit, imposed by regulatory entities, for all except two samples that showed an indoor dose value of 1.68 mSv/y and 1.95 mSv/y.

Keywords: Phosphogypsum, Gypsum shortage, IBA, Radiological Risk Assessment

Resumo

Fosfogesso (PG) é o principal subproduto do processamento húmido de rocha fosfatada, durante o fabrico de ácido fosfórico. Estimativas apontam para uma produção anual de 100 a 280 milhões de toneladas, existindo perto de 6 mil milhões de toneladas disponíveis mundialmente. Dada a crescente procura por materiais à base de gesso para aplicações agrícolas e industriais e a previsível escassez de gesso nas próximas décadas, o PG pode ser uma opção para preencher este mercado.

Elevadas concentrações de radionuclídeos das séries de decaimento do urânio-238 e tório-232 e de flúor limitam a possibilidade de utilização do PG, dados os efeitos negativos que estes contaminantes podem ter na saúde e no meio ambiente. O objetivo deste trabalho, enquanto parte do projeto PG2CRM, foi caracterizar quimicamente amostras de PG para ajudar a desenvolver técnicas que permitam purificá-lo, de forma a que possa ser utilizado como matéria-prima de baixo custo.

Dezassete amostras, provenientes da Alemanha e França, foram analisadas com recurso a PIGE, PIXE e EBS. O uso destas técnicas permite fazer uma caracterização extensiva das amostras, com destaque para o flúor, por ser extremamente difícil de quantificar com outros métodos de análise, e REE, dada o seu elevado valor económico caso sejam extraídos do PG.

Os resultados mostraram elevadas quantidades de cálcio (26 wt.%-29 wt.%) e enxofre (19.4 wt.%-23.8 wt.%). Sódio, alumínio, silício, titânio, ferro e estrôncio estavam presentes em baixa concentração (até 2 wt.%). Alguns valores atípicos foram encontrados para elementos como fósforo e cloro, que apresentaram concentrações elevadas em algumas amostras. Estes valores foram atribuídos aos tratamentos previamente aplicados às amostras. As concentrações de flúor variaram entre 0.003 wt.% e 0.691 wt.%, sendo que até os valores mais baixos ultrapassam os limites de concentração impostos para contaminação de águas e utilização na indústria do gesso. A deteção de REE não foi significativa, tendo sido observadas apenas pequenas concentrações de cério e gadolínio.

A avaliação de risco radiológico mostrou que as amostras tinham concentrações baixas de radionuclídeos, com uma atividade equivalente de rádio média de 265.04 Bq/kg e valores de 0.89, 0.72 e 1.29 para índices gamma, externo e interno, respetivamente. As doses anuais efetivas, avaliadas no interior e exterior, estavam abaixo do limite de 1 mSv/y, imposto pelas entidades reguladoras, em todas exceto duas amostras, que apresentaram um valor de dose efetiva de 1.60 mSv/a e 1.95 mSv/a.

Palavras-chave: Fosfogesso, Escassez de gesso, IBA, Avaliação de Risco Radiológico

Contents

List of Figures viii

List of Tables ix

Acronyms x

1 Introduction 1

2 Contextual Background 3

2.1 Phosphogypsum . . . 3

2.2 Environmental Impact of Phosphogypsum . . . 5

2.2.1 Contamination Sites: A Representative Case . . . 6

2.3 Repurposing Phosphogypsum . . . 7

2.3.1 Decontamination and Extraction Methods . . . 7

2.3.2 Evaluation of Decontamination Efficacy . . . 8

3 Ion Beam Analysis 9

3.1 Charged Particle Interaction with Matter . . . 9

3.1.1 Energy Loss and Stopping Power . . . 10

3.2 Elastic Backscattering Spectrometry (EBS) . . . 11

3.3 Radiation Interaction with Matter . . . 12

3.3.1 Intensity Attenuation . . . 12

3.4 Particle Induced X-ray Emission (PIXE) . . . 12

3.5 Particle Induced Gamma-ray Emission (PIGE) . . . 13

4 Experimental Setups 14

4.1 3 MV Tandem Accelerator . . . 15

4.1.1 Beam Creation and Optimization . . . 15

4.1.2 Reaction Chamber and Detection System . . . 15

4.2 2.5 MV Van de Graaff Accelerator . . . 16

4.2.1 Nuclear Microprobe . . . 17

4.3 Sample Preparation and Measurement . . . 18

5 Analysis of Sample Composition 19

5.1 Elemental Matrix and Charge Collection . . . 19
5.1.1 Spectra Simulation with NDF . . . 20
5.1.2 Excitation Function Calculations . . . 21
5.2 Light Element Quantification . . . 22
5.3 Heavy Element Quantification . . . 24
5.3.1 Elemental mapping . . . 25
5.4 Comparative Analysis of All Acquired Data . . . 26

6 Radiological Risk Assessment **30**
6.1 Radionuclide Activities in Building Materials . . . 30
6.1.1 Radium-226 . . . 30
6.1.2 Potassium-40 . . . 31
6.1.3 Thorium-232 . . . 31
6.2 Parameters for Classification of Building Materials . . . 32
6.2.1 Gamma Index . . . 32
6.2.2 Radium Equivalent Activity . . . 32
6.2.3 Hazard Indexes . . . 33
6.2.4 Cross-Comparison of Radiological Risk Data . . . 33
6.3 Radiation Exposure . . . 34

7 Conclusions **36**

Bibliography **37**

Appendices

A Complete EBS and PIXE Data **41**

List of Figures

2.1 Phosphogypsum stockpile satellite images. Retrieved using Google Maps. 5
2.2 Uranium-238 decay series. Retrieved from [10]. 6

3.1 Four outcomes of charged particle interaction with matter. 10
3.2 Stopping power curves for various elements, commonly found in PG. Obtained using data from SRIM [33]. 11

4.1 Accelerator room plan at the LATR. Retrieved from [36]. 14
4.2 Exterior and interior views of the NRA beamline reaction chamber. 16
4.3 Exterior view of the nuclear microprobe reaction chamber. 17
4.4 Loaded sample holder and compressed PG pellets. 18

5.1 EBS spectrum of sample L1g, with main scattering barriers identified. 20
5.2 Obtained ^{23}Na excitation function for energies between 2 and 4 MeV compared to results published by other authors [38, 39]. 22
5.3 PIGE spectrum of sample L1g. 23
5.4 PIXE spectrum of sample PgP, at 2020 keV beam energy. 24
5.5 PIXE spectrum of sample PgP, at 700 keV beam energy. 25
5.6 Maps of elemental distribution obtained with the nuclear microprobe, for sample L1g. 26

6.1 Average activity of ^{226}Ra, ^{40}K and ^{232}Th in building materials. Retrieved from [42]. 31

List of Tables

2.1 PG average major element composition. Adapted from [3]. 4
2.2 REE content in phosphogypsum from Wizów, Poland. Adapted from [4]. 4
2.3 Average ^{226}Ra activity in multiple PG deposition sites. 6

5.1 Most relevant gamma spectrum nuclear reactions for sample L1g. 23
5.2 Elemental composition of all analysed samples, obtained using PIGE. 28
5.3 Elemental composition of all analysed samples, obtained using PIXE, with 2020 keV beam energy. 29
5.4 Elemental composition of all analysed samples, obtained using PIXE, with 700 keV beam energy. 29

6.1 Activity in PG samples, for the most important radionuclides in construction raw materials. 31
6.2 Radium equivalent activity, Gamma Index and Hazard Indexes for all the analysed samples. 33
6.3 Comparison of Radium equivalent dose, Gamma Index and Hazard Indexes between the average of the analysed samples and other building materials [42]. 34
6.4 Absorbed doses and annual effective doses for different exposure conditions. 35

A.1 Elemental composition obtained using EBS (pp. 42, 43) 42
A.2 Elemental composition and associated fitting error percentage obtained using PIXE, with 2020 keV beam energy. 44
A.3 Elemental composition and associated uncertainties obtained using PIXE, with 700 keV beam energy. 45

Acronyms

ADC Analogue to Digital Converter *(p. 18)*
AED Annual Effective Dose *(pp. iv, 34)*

CTN-IST Nuclear and Technological Campus of Instituto Superior Técnico *(pp. 1, 14)*

EBS Elastic Backscattering Spectrometry *(pp. iv, v, 1, 10, 11, 14, 19, 20, 22, 24, 26, 36, 41)*
EU European Union *(pp. 1, 4)*

FGD flue gas desulphurization *(p. 4)*
FTIR Fourier Transform Infrared Spectroscopy *(p. 8)*

HE high energy *(p. 15)*
HPGe High Purity Germanium *(pp. 15, 16)*

IAEA International Atomic Energy Agency *(p. 35)*
IBA Ion Beam Analysis *(pp. 1, 36)*
ICP-MS Inductively Coupled Plasma Mass Spectrometry *(p. 8)*
ICRP International Commission on Radiological Protection *(p. 34)*

LATR Laboratory of Accelerators and Radiation Technologies *(pp. 1, 14, 21)*
LE low energy *(p. 15)*

NORM Naturally Occurring Radioactive Material *(p. 33)*
NRA Nuclear Reaction Analysis *(pp. 14, 15, 17)*

PG Phosphogypsum *(pp. iv, v, 1, 3–7, 19, 20, 27, 30, 36)*
PG2CRM Phosphogypsum Processing to Critical Materials *(pp. iv, v, 5, 19, 36)*
PIGE Particle Induced Gamma-ray Emission *(pp. iv, v, 1, 8, 11–14, 20, 22, 24, 26, 27, 36, 41)*
PIPS Passively Implanted Planar Silicon *(pp. 15, 16, 21)*
PIXE Particle Induced X-ray Emission *(pp. iv, v, 1, 8, 11–14, 20, 24, 25, 27, 36, 41)*

REE rare-earth elements *(pp. iv, v, 4, 5, 7, 19, 27, 36)*

ROI region of interest *(p. 23)*

SDD Silicon Drift Detector *(p. 17)*

TENORM Technologically Enhanced Naturally Occurring Radioactive Material *(p. 4)*

UNSCEAR United Nations Scientific Comitee on the Effects of Atomic Radiation *(p. 32)*
USEPA United States Environmental Protection Agency *(p. 6)*

XRD X-ray Diffraction *(p. 8)*
XRF X-ray Fluorescence *(p. 8)*

CHAPTER 1

INTRODUCTION

The present work aims to add value to the ongoing efforts to better chemically characterize PG and understand how its current methods of treatment can be improved, in order to minimize environmental risks. Moreover, with a rise in demand for gypsum based materials, to be used in industrial applications, an in-depth knowledge of the current dangers incurred with phosphogypsum deposition in stockpiles, and possible solutions for this matter, can be of paramount importance. For that, Ion Beam Analysis (IBA) techniques were conducted on multiple samples, from different provenances, taking advantage of matter interaction with a high-energy proton beam, generated in the particle accelerators available at the Nuclear and Technological Campus of Instituto Superior Técnico (CTN-IST).

The work will be structured as follows. A general overview on the worldwide phosphogypsum production, treatment and storage will be presented in chapter 2. This aims to contextualize the reader on the typical methods used within this industry. Based on [2] and similar works, a case will be made for a predictable increase in gypsum necessity, especially within the European Union (EU). This, in turn, solidifies the need for the repurposing of phosphogypsum. The ability to use phosphogypsum as a viable construction material can prove to be a step in the right direction environmentally, as it would not only allow for toxic stockpiles to be eliminated, as well as aid in the reduction of fossil fuel consumption. Subsequently, phosphogypsum's main constituents will be listed, and its toxicity will be justified. Chapter 3 will detail on the experimental methods used for sample analysis, as well as the underlying physical principles that rule over high energy particle collisions. This will also include a description of the setups available at the Laboratory of Accelerators and Radiation Technologies (LATR) at CTN-IST, in chapter 4. Two accelerators were used to perform PIXE, PIGE and EBS on all available samples. Chapter 5 will make use of all of the gathered data and assess sample composition and quantification. Correlations can then be made between the treatment applied to each sample, and its efficacy in decontaminating the material. Finally, in chapter 6, a radiological risk assessment will be performed, in order to evaluate

the potential health and environmental risks of using contaminated phosphogypsum in a multitude of situations.

The research work described in this dissertation was carried out in accordance with the norms established in the ethics code of Universidade Nova de Lisboa. The work described and the material presented in this dissertation, with the exceptions clearly indicated, constitute original work carried out by the author.

This work is financed by national funds through the FCT - Fundação para a Ciência e Tecnologia, I.P., within the scope of the Project ERA-MIN3/0008/2021 PG2CRM - “Phosphogypsum processing to critical materials”.

CHAPTER 2

CONTEXTUAL BACKGROUND

This chapter will contextualize the work done, detailing on the current life cycle of phosphogypsum, describing its production, storage methods, possible applications and treatments. Additionally, the environmental risks associated with large phosphogypsum stockpiles will be clarified. This will provide not only better insight into the characteristics of this material, as well as justify the chosen physical analysis methods, which are later explained.

2.1 Phosphogypsum

Phosphogypsum is an off-white granular powder, originating mainly as a by-product of phosphoric acid production. With an ever-increasing population, the world has experienced a steep rise in the necessity for large quantity, fast growth foods and, with that, an enormous rise in demand for phosphoric acid based fertilizers.

The most common process by which phosphoric acid is produced involves chemical reaction 2.1. Given its stoichiometry, for every tonne of phosphoric acid produced, around five tonnes of phosphogypsum are generated.

$$Ca_5(PO_4)_3F_{(s)} + 5\,H_2SO_{4(aq)} + 10\,H_2O_{(aq)} \rightarrow 5\,CaSO_4 \cdot 2H_2O_{(s)} + 3\,H_3PO_{4(aq)} + HF_{(g)} \quad (2.1)$$

Phosphogypsum's elemental composition is strongly influenced by the parent phosphate rock from which it originates, as well as production-process factors. As such, both in the reviewed literature and in the results presented in chapter 5, significant fluctuations in sample composition can be observed. Nevertheless, it is mainly composed of calcium sulphate dihydrate, silicates, and iron and phosphorous oxides [3, 4]. Table 2.1 shows the average major element composition of PG. More worrying are the high quantities of fluorides, traced back to the fluorapatite present in the rock, and the common presence of radionuclides of the uranium-238 (^{238}U) and thorium-232

(^{232}Th) decay series. Due to its radioactivity, phosphogypsum is classified as a Technologically Enhanced Naturally Occurring Radioactive Material (TENORM).

Table 2.1: PG average major element composition. Adapted from [3].

Component	Concentration (wt.%)	Component	Concentration (wt.%)
CaO	25-32.13	Fe_2O_3	0.03-0.9
SiO_2	0.29-9.5	SO_3	37.60-58
Al_2O_3	0.10-2.8	F^-	0.15-1.20

Additionally, phosphogypsum is also a potential source of REE and other trace metals, and the possibility of extracting these elements from the material, prior to its utilization, should not be discarded. Table 2.2 shows the concentration of some elements on an REE rich phosphogypsum.

Table 2.2: REE content in phosphogypsum from Wizów, Poland. Adapted from [4].

Elements	Concentration (mg/kg)	Elements	Concentration (mg/kg)
Cerium	2036-2234	Neodymium	685.9-752.5
Gadolinium	117.2-128.6	Praseodymium	200.5-220.0
Lanthanum	1408-1545	Samarium	97.4-106.8

The yearly worldwide production of PG is estimated to about 100-280 million tonnes [4]. As of 2022, around 2 billion tonnes of phosphogypsum were stored and readily available for use within the EU alone, with a worldwide availability amounting to close to 6 billion tonnes [2]. Furthermore, the main method of common gypsum production, within the EU, is through flue gas desulphurization (FGD) in coal-fired power plants [5]. This process is described in equation 2.2. With ongoing efforts towards abandoning fossil fuels in the coming decades, gypsum availability will gradually decrease. The results of coal burning power plant closures, and its effect on gypsum production, have the potential to affect 21 EU countries directly and the remaining indirectly [2].

$$SO_{2(g)} + CaCO_{3(s)} + 2\,H_2O_{(aq)} \rightarrow CaSO_4 \cdot 2H_2O_{(aq)} + CO_{2(g)} \tag{2.2}$$

Moreover, predictions point to an increase in soil salinization, brought along by climate change, which will increase the need for the use of gypsum as soil amendment. Projections show that the quantity of PG needed for this purpose could catch up to the level now being used in construction, as early as 2040 [6].

However, this high output of PG at phosphoric acid production plants, associated with the material's composition, makes it so that, nowadays, only around 10% to 15% of its total is recycled for other applications [3]. The remaining 85%, which could amount to more than 200 million tonnes per year, is classified as waste, and disposed of untreated. The increasing demand for gypsum-based materials, combined with a huge surplus of phosphogypsum, makes it imperative to find safe and economically viable ways of repurposing more of the latter, as it could generate financial benefits and reduce its environmental footprint.

(a) Sfax, Tunisia (b) Kutina, Croatia (c) Huelva, Spain

Figure 2.1: Phosphogypsum stockpile satellite images. Retrieved using Google Maps.

The aim of the experiments within the PG2CRM project, of which the present work is a part of, is to develop techniques that allow purification of the $CaSO_4$ (gypsum) phase, utilizing the extracted impurities for other purposes, enabling the use of PG as an inexpensive material for construction and agriculture.

2.2 Environmental Impact of Phosphogypsum

The lack of low-cost, suitable storage alternatives or recycling possibilities meant that, over the last decades, tonnes of material have been disposed of into the ocean or accumulated in massive stockpiles. Depending on each region's legislation, stockpiles have various degrees of monitoring and proximity to populations, water bodies or other potentially dangerous locations. Figure 2.1 shows three examples in Europe and Northern Africa.

Regardless of how tightly controlled the stacks are, environmental and health risks do exist. Primary concerns include the release of radioactive species, such as radon-222 (^{222}Rn), from the alpha decay of radium-226 (^{226}Ra), into the atmosphere and the leaching of mobile elements, such as REE, fluorine and even phosphorus. Given the common occurrence of open pit stockpiles, the incorporation of these elements in water sources and soils is very likely. If present in high enough concentration, these substances lead to undesirable effects, including heavy metal poisoning, internal organ damage, due to radon inhalation, or even high algae blooms in water bodies [7]. Fluorine, although beneficial if used carefully, can cause dental and skeletal fluorosis and an elevated risk of bone fractures and crippling deformities, if ingested in high quantities or if exposed to, over a long period of time [8]. In the construction industry, gypsum with fluorine contents above 10 mg/kg is banned from use in calcination furnaces, due to the accumulation of hydrogen fluoride in the system, which can be highly corrosive.

As aforementioned, most of the radioactive species present in PG pertain to the ^{238}U decay series (figure 2.2). Due to solubility differences, uranium tends to migrate to phosphoric acid and its daughter isotopes accumulate in phosphogypsum, making them the main cause of elevated activity. The ratio of activity in a sample, between ^{238}U and ^{226}Ra, can go from 1:1 in phosphate rock to 1:2 in PG [9].

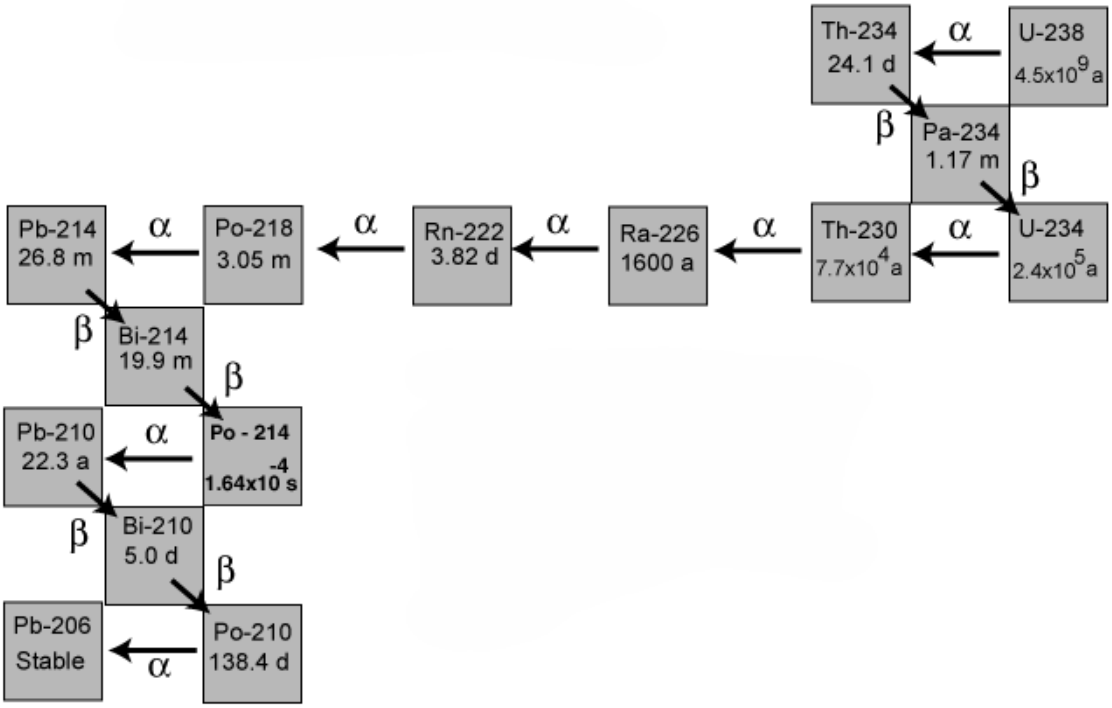

Figure 2.2: Uranium-238 decay series. Retrieved from [10].

Stockpiles have been measured to have a mean ^{226}Ra activity of up to 1420 Bq/kg, in Moroccan PG [11], with some aggregates from the Barreiro stockpile (Portugal) reaching 5000 Bq/kg [12] (stockpiles are, generally, very heterogeneous). Table 2.3 shows ^{226}Ra activity for various sites. As a reference, the United States Environmental Protection Agency (USEPA) banned the use of phosphogypsum with activity exceeding 370 Bq/kg and ^{222}Rn exhalation over 0.74 Bq/m^2/s.

Table 2.3: Average ^{226}Ra activity in multiple PG deposition sites.

Location	Activity (Bq/kg)	Reference	Location	Activity (Bq/kg)	Reference
Morocco	1420	[11]	Portugal	735	[12]
Canada	890	[13]	Spain	800	[14]
Brazil	600	[15]	USA	900	[16]
Syria	300	[17]	Egypt	100	[18]

2.2.1 Contamination Sites: A Representative Case

Phosphogypsum stacks in southwestern Spain have been measured to have a local radiation level of up to 38 times the normal soil rate. Nine minutes per day of exposure to the radiation emitted by a 1 m^2 patch of material would be equivalent of around 4 times the recommended yearly exposure limit of 1 mSv [3].

It is also known that most heavy metals have a high transferability from phosphate rock to PG and then onto surrounding waters. Studies conducted in Huelva, Spain show that, for a 100 million

tonne PG stack, as much as 52 219 tonnes of elements, such as the barium, zinc, nickel, copper, cadmium and strontium, may be released into the nearby river [19].

Another study carried out in the same area showed that the surrounding estuary waters were severely contaminated by U-series radionuclides. Collected samples presented an elevated level of polonium-210 (^{210}Po) activity, with a value of 10 ± 3 mBq/l (with the typical activity in uncontaminated estuary waters being 2 mBq/l) [20].

2.3 Repurposing Phosphogypsum

In recent years, mainly due to an increase in production volume and anthropogenic pressure on the environment, a growth in the interest for broader applications for PG has been observed [21]. For that reason, despite its toxicity, there are ongoing efforts to repurpose this material for soil amendments and a variety of other industrial processes. For example, as a cement additive, it has been shown to improve setting times, compression strength and resistance to fluid infiltration. It has also showed promise as a low-cost, fire resistant alternative to bricks and plasterboard [22] and a viable option to incorporate in asphalt deposition [23]. Other studies [24–28] confirm the applicability of PG, after undergoing diverse treatments, as substitute for natural gypsum in a multitude of situations.

In order to maximize not only environmental, but also economic benefits, one should have in consideration the removal of all constituents that may be detrimental, as well as all those that can be used independently for other applications. In addition, the products resulting from decontamination and extraction should be analysed, in order to assess their own environmental consequences. One particular method can be extremely efficient in impurity removal, but if the generated waste is also toxic, or if the process is not economically attractive, then the method is sure to be abandoned.

2.3.1 Decontamination and Extraction Methods

A variety of methods have been proposed by researchers to render PG ready for later applications. These generally consist in washing, sieving, lime neutralisation or leaching with acidic solutions (commonly sulphuric acid).

The most common method consists in using a leaching solution to wash away both major and trace elements, present in the samples. Using ultra-pure water as a solvent can reduce Ca, S and P concentrations in 22%, 13% and 43%, respectively [29]. Other constituents like REE and low concentration impurities are also removable, although more retained in the PG matrix, requiring stronger chemical leaching. Even so, Al-Masri et al. [30] were able to remove U (31%), Cd (25%), Zn (10%) and Cu (10%) using an H_2SO_4 solution. It was also shown that increasing the acid's concentration resulted in an increase in leaching efficiency.

More promising results, yielding a higher extraction percentages, can be achieved using organic compounds in kerosene, as presented by El-Didamony et al. [31]. Radionuclides of the ^{238}U series had an extraction percentage between 83.4% and 92.1%. The same process also achieved an 80.1% average extraction percentage for REE.

2.3.2 Evaluation of Decontamination Efficacy

With an ever-growing number of decontamination and element extraction methods one thing stands to be performed on all samples: an elemental composition analysis to evaluate the treatments efficiency. Techniques frequently used include Inductively Coupled Plasma Mass Spectrometry (ICP-MS), X-ray Diffraction (XRD), X-ray Fluorescence (XRF), Raman Spectroscopy, Fourier Transform Infrared Spectroscopy (FTIR), among others. Less used, but with enormous potential are the nuclear techniques used within the scope of this work: PIXE, PIGE and EBS. Their advantages and how they were applied to the study of phosphogypsum will be detailed in the following chapters.

CHAPTER 3

Ion Beam Analysis

The current chapter will set forth an overview of the main types of interactions between matter and charged particles, and their probable outcomes. Subsequently, the techniques used to obtain the results presented in this work will be detailed, as well as the information that may be extracted from analysing particle collision data.

3.1 Charged Particle Interaction with Matter

When studying matter interaction with charged particles, two forces and two types of collision must be taken into account: Coulomb and nuclear forces; elastic or inelastic collisions. Although the physical principles here presented are valid for any type of charged particle, from now on protons will be considered, since they were used to acquire all the data within the scope of this work.

Both elastic and inelastic interactions, between incident protons and atomic electrons, are very common and can generate multiple outcomes. If the energy transferred to the electrons is within range of the atom's electronic transitions, excitation might occur. Moreover, if energy is above a defined threshold, ionization, upon which the subsequently presented techniques rely, may happen. Another possibility is the emission of *bremsstrahlung*, with proton deceleration. This process is, however, only relevant for energies much higher than the ones used for this work. This is due to protons being about two thousand times heavier than electrons, greatly reducing the probability of proton-induced *bremsstrahlung*.

The protons can also interact electrostatically with the nuclei of the target sample resulting in scattering, which is well described by the Rutherford cross-section formula if the process is due exclusively to Coulomb forces. Furthermore, if the proton's energy is high enough, it may break through the Coulomb barrier, imposed by the repulsive force of the positively charged nucleus (expressed in equation 3.1, where Z_1 and Z_2 are the atomic number of the projectile and target, R_1 and R_2 their respective radii) [32]. This is possible even at lower energies, through quantum

tunnelling, although much rarer.

$$V_C = \frac{e^2}{4\pi\varepsilon_0}\frac{Z_1 Z_2}{R_1 + R_2} \tag{3.1}$$

The proton will then be close enough (distance similar to the sum of the nuclear radii of the involved particles) for nuclear forces to come into play. The nuclei can elastically scatter the incoming proton, deflecting it from its original path. A similar process can occur with energy transferred from the incoming proton to the nucleus, leaving it in an excited state. Similarly to what can happen with electron rearrangement, the relaxation of nuclei when transitioning to a lower energy level is key for the analysis here conducted. Alternatively, a nuclear reaction might occur, where the collision between the proton and the resting nucleus generates a different species of atom and emitted particle. Figure 3.1 illustrates these processes.

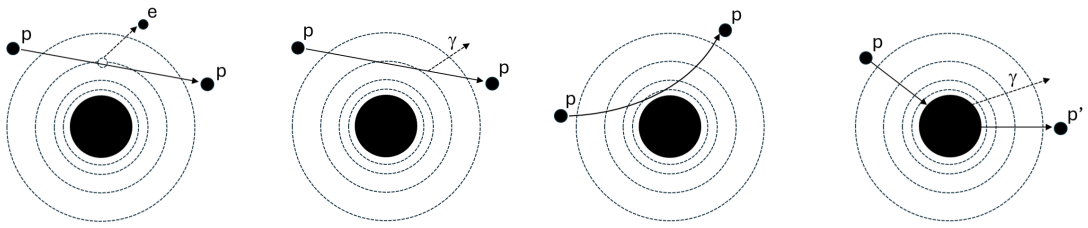

(a) Ionization (b) *Bremsstrahlung* (c) Elastic nuclear (d) Nuclear reaction

Figure 3.1: Four outcomes of charged particle interaction with matter.

3.1.1 Energy Loss and Stopping Power

As protons penetrate and travel through a material, they lose energy in the aforementioned processes. This means than a particle fired into a target will have a limited range of penetration and will stray off its original trajectory. The rate at which a particle travelling through matter loses energy is defined as the material's stopping power (equation 3.2).

$$S = -\frac{dE}{dx} \tag{3.2}$$

The stopping power is dependent on the characteristics of the target material and the energy of the projectile particle. The higher the electronic density of the material, the higher its stopping power will be, limiting the range of the projectile. Also, a higher projectile energy will increase the penetration distance. As an example, figure 3.2 shows the characteristic stopping power curves for protons in various materials. This concept will be crucial to accurately interpret results, obtained with the subsequently mentioned nuclear analytical techniques, particularly EBS.

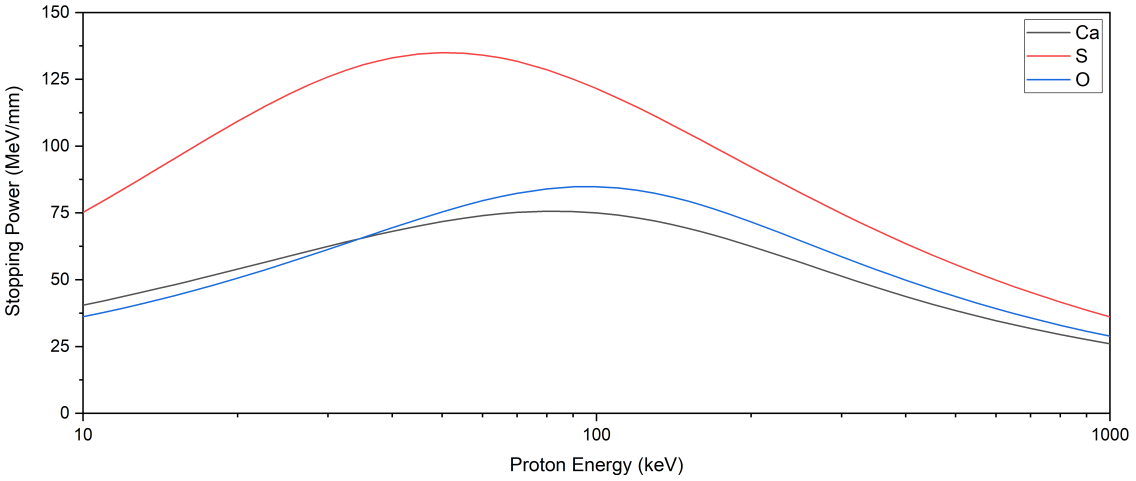

Figure 3.2: Stopping power curves for various elements, commonly found in PG. Obtained using data from SRIM [33].

3.2 Elastic Backscattering Spectrometry (EBS)

In order to facilitate and complement the analysis performed with PIXE and PIGE, EBS is commonly used. This technique allows not only for sample composition analysis, as well as depth profiling, up to a few dozen micrometres, with high sensitivity and no need for standard sample use. As the name suggests, it works by bouncing protons off a target material and measuring their energy when reaching the detector, after the collision. It is known that the energy of a rebounding proton will be dependent on the atomic composition of the sample it collides with. Mathematically, in an elastic collision, the energy carried by the proton, after the collision, is equal to its initial energy multiplied by a factor, K, defined as the collision's kinematic factor. This quantity is dependent exclusively on the masses of the projectile and target particles, and the scattering angle (see equation 3.3, where M_1 is the projectile mass, M_2 the target mass and θ the angle [34]).

$$K = \left(\frac{(M_2^2 - M_1^2 \sin^2 \theta)^{1/2} + M_1 \cos \theta}{M_1 + M_2} \right)^2 \tag{3.3}$$

In addition, if a proton is backscattered at depth, it will lose energy, not only in the rebound towards the detector, but also while travelling within the target material, as per the process described in subsection 3.1.1. Combining this information, a precise measurement of sample composition and depth distribution of the constituent elements can be made. Equation 3.4 defines the energy losses in the process (E_{final} being the energy when reaching the detector, E_0 the initial energy and ΔE_{in}, ΔE_{out} the energy lost travelling through the target medium, before and after the scattering, respectively).

$$E_{\text{final}} = K\,(E_0 - \Delta E_{\text{in}}) - \Delta E_{\text{out}} \tag{3.4}$$

The probability of the occurrence of backscattering is defined as the collisions cross-section, which is dependent on the energy of the collision, masses and atomic numbers of the elements

involved and the scattering angle. For the parameters of the analysed samples, significant deviations from the values given by the Rutherford cross-section calculations, as given by equation 3.5 (where Z_1, M_1 and Z_2, M_2 are the atomic number and mass of the projectile and target, respectively, E the collision energy, θ the scattering angle and e a constant), are observed. As such, published experimental cross-section values, for the necessary elements, were used to ensure an accurate analysis.

$$\sigma_{\text{Ruth.}} = \left(\frac{Z_1 Z_2 e^2}{4E}\right)^2 \frac{4}{\sin^4\theta} \frac{\left(\cos\theta + \sqrt{1-(M_1/M_2)^2\sin^2\theta}\right)^2}{\sqrt{1-(M_1/M_2)^2\sin^2\theta}} \tag{3.5}$$

3.3 Radiation Interaction with Matter

In order to interpret the spectra generated with PIGE and PIXE, a few concepts, regarding the interaction of radiation with matter, must be addressed. These will help to clarify some of the structures later observed when analysing the obtained results.

3.3.1 Intensity Attenuation

As photons travel through a material their intensity is attenuated exponentially, in a process described by the Lambert-Beer law (equation 3.6, where I_0 is the initial intensity, μ is the linear attenuation coefficient and x the distance travelled within the material). This means that the higher the distance travelled by the photon, through the target material, the less the corresponding peak will be visible in the radiation spectra. This can difficult the detection of some elements present in a sample and should be taken in consideration when treating the results.

$$I(x) = I_0 \exp(-\mu x) \tag{3.6}$$

The linear attenuation coefficient is calculated based on the cross-sections of the different processes occurring when a photon traverses a medium: photoelectric effect, Compton scattering and pair production (see equation 3.7, where N is the atomic density and σ_{Total} the total cross-section of the aforementioned processes).

$$\mu = N\sigma_{\text{Total}} \tag{3.7}$$

3.4 Particle Induced X-ray Emission (PIXE)

PIXE is a powerful, non-destructive analytical technique, that allows for fast and simultaneous detection of major, minor and trace elements in a sample. It is based on a simple two-step process.

When a beam of particles, in this case protons, collides with a material, as explained in section 3.1, the energy transfer from protons to electrons can cause ionization. If the incident protons carry enough energy, electrons from the inner most shells (K and L) of the atoms can be ejected. This leaves behind an exited atom with a vacancy in its core layers. In order to return to

a lower energy configuration, an electron from a higher energy level will migrate to the available inner shell hole. For energy to be conserved, a photon is emitted whenever the electrons rearrange themselves. The energy of the emitted radiation will be equal to the difference between the level from which the electron came to the level it is going to occupy. This energy is characteristic of the chemical element responsible for the emission of the radiation and can be easily measured. This allows for element identification. Furthermore, it is possible to quantify the amount of a certain element, present in a sample, by measuring the intensity of the radiation emitted. Evidently, the higher the number of atoms of a certain species, more ionizations will occur and, consequently, more radiation will be emitted.

3.5 Particle Induced Gamma-ray Emission (PIGE)

PIGE is also a non-destructive, multi-element analysis technique. However, contrary to PIXE, which relies exclusively on electrostatic interactions, PIGE combines a nuclear reaction followed by relaxation of the resulting nucleus. For example, a proton collides inelastically with a nucleus. Some energy is transferred from the proton to the nucleus, leaving it in an excited state. Subsequent de-excitation occurs with gamma radiation emission. Similarly to what happens in PIXE, the radiation emitted is characteristic of the nucleus from which it originates. That can be measured and used to identify the isotopic composition of a sample, as well as do element quantification using gamma radiation intensity.

Due to the increasing Coulomb repulsion force with the increase of atomic number, the cross-sections for this type of reaction fall abruptly when moving towards heavier elements. For that reason, PIGE is mainly used for light elements (typically, with max. $Z \approx 20$).

CHAPTER 4

EXPERIMENTAL SETUPS

Electrostatic accelerators have come a long way since being introduced, in 1932, by Cockcroft and Walton [35]. The improvements made to these machines, has allowed for the precise control of beam energy, intensity and particle mass. This has assured that they continue to be at the forefront of atomic and nuclear physics, enabling the study of phenomena in a broad range of situations. This chapter will analyse the specifics of the setups utilized within the scope of this work.

All measurements performed and presented were conducted using the machines at the LATR, within CTN-IST (as seen in figure 4.1). Both available electrostatic accelerators were used: the Van de Graaff accelerator was used to perform PIXE, in the nuclear microprobe beamline; the Tandem accelerator was used to perform PIGE, in the Nuclear Reaction Analysis (NRA) line. EBS was performed on both setups.

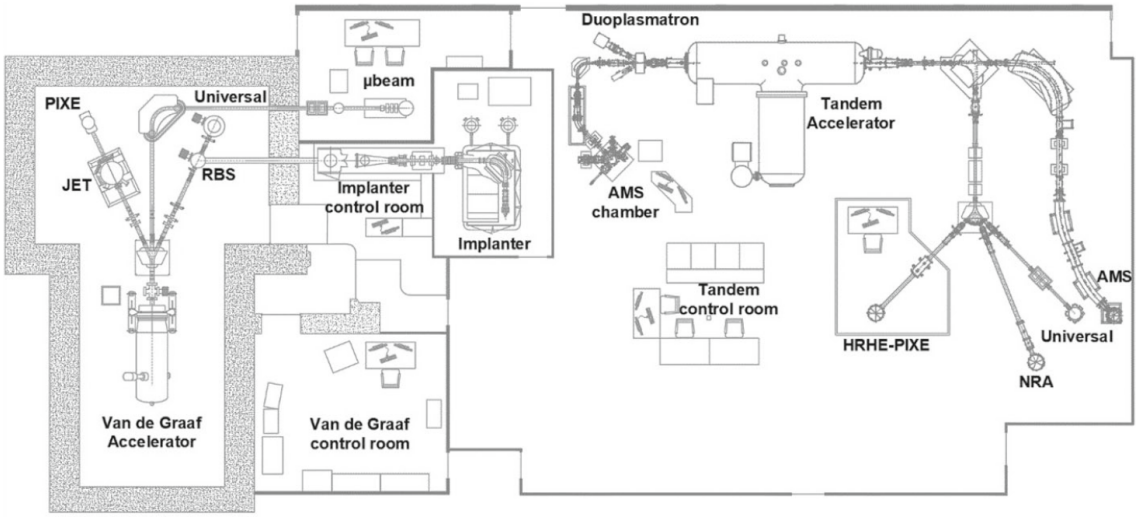

Figure 4.1: Accelerator room plan at the LATR. Retrieved from [36].

4.1 3 MV Tandem Accelerator

As the name suggests, the Tandem accelerator is a two-stage machine, which uses the same high voltage terminal to accelerate charged particles twice. This is an efficient way of producing a high energy, stable beam. Its working principle can be divided into low energy (LE) and high energy (HE) sections, as outlined below.

4.1.1 Beam Creation and Optimization

A steady ion beam is produced using a Duoplasmatron H^- source, where a plasma is created from the interaction of free electrons with a molecular gas. Ions are extracted from the plasma through an arrangement of charged grids forming an ion beam, with an energy of 15 keV. The negatively charged ions are then accelerated towards the high voltage terminal, incorporating a Cockcroft-Walton type generator. On its way, the ion beam passes through a switching magnet that filters ions based on their mass to charge ratio. Upon entering the high voltage tank, the beam goes through a low-pressure gas. The collision between the hydrogen anions and the gas molecules will ionize the H^-, making the beam now positively charged. This marks the end of the LE stage.

Given this charge exchange, the same potential that initially attracted the negative ions into the voltage terminal, is now repulsive to the positively charged proton beam. The HE stage begins, as this repulsion significantly increases the proton beam's energy, which now shoots off the other side of the tank with energies of up to a few MeV. The beam then passes through a variety of beam optimization devices. These consist of electrostatic quadrupoles, a 90° analysing magnet and a switching magnet, that directs the beam into the NRA beamline. Faraday cups are placed both in the LE and HE sections, as well as in the NRA chamber in order to measure beam current at different points of the beamline. This is used to optimize beam current in each of the system's stages and help guide it towards the sample.

4.1.2 Reaction Chamber and Detection System

After travelling through the aforementioned stages, the beam reaches the reaction chamber (exterior and interior views in figure 4.2). Inside, a height adjustable sample holder suspends the samples in the path of the proton beam. In order to facilitate beam guidance and focusing, a fluorescence target is placed in the holder, along with the first batch of samples. A camera is pointed at the sample holder, through a window in the reaction chamber wall, which is then covered to prevent external lighting from interfering with the particle detectors. Given the high sensitivity of the beam adjustment magnets, making the beam reach the desired sample can be a difficult task. The fact that the fluorescence target lights up, when hit by the beam, makes it easier to fine tune the setup parameters.

Two of the three detectors available in this setup were used: a High Purity Germanium (HPGe) detector for gamma radiation and a Passively Implanted Planar Silicon (PIPS) detector for scattered charged particles, protons in this case. Nowadays, HPGe detectors are typically favoured for gamma radiation detection due to their high efficiency and far better resolution, when compared to other

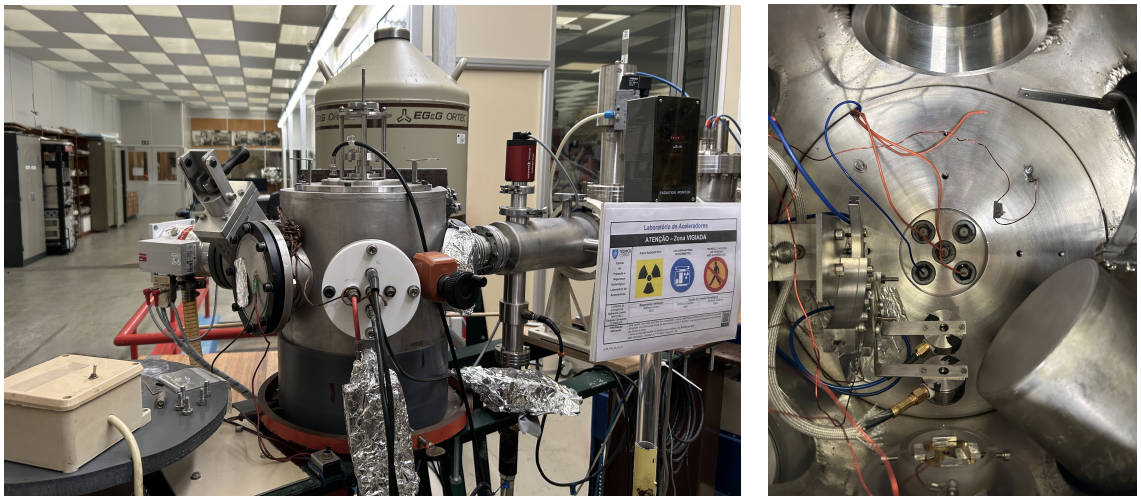

(a) Exterior view (b) Interior view

Figure 4.2: Exterior and interior views of the NRA beamline reaction chamber.

contenders, such as sodium iodine scintillation counters. They are made by growing a highly pure germanium crystal and using it to create an electronic junction. The material's low impurity concentration helps reduce the noise. They need, however, to be operated at cryogenic temperatures, to minimize the numbers of thermally generated charge carriers, hence the liquid nitrogen reservoir seen in figure 4.2.

When a photon enters the detector, it interacts with the semiconductor material through three distinct mechanisms: photoelectric effect, Compton scattering and electron-positron pair production. All three create observable structures in the resulting spectrum and, as such, should be accounted for. The number of created electron-hole pairs is proportional to the energy deposited in the detector by the interacting photon. A higher energy photon will deposit more energy, creating more pairs, which will, in turn, generate a higher current pulse.

Proton detection is achieved using a PIPS detector. Similarly to HPGe detectors, a planar high purity silicon device is created. Controlled impurity doping creates an electronic junction. The energy deposited by the protons, in the detector material, will create charge carriers that are then mobilized by an electric field, allowing for particle detection.

4.2 2.5 MV Van de Graaff Accelerator

Though often used for similar purposes, the working principle of the Van de Graaff accelerator differs from that of the Tandem accelerator, explained in section 4.1. In the case of the Van de Graaff, charge generation is achieved using a belt, made from an electrically insulating material, and two rollers inside a conducting hollow sphere, where an ionizing gas discharge happens. This electrical discharge can be altered to create either positive or negative free charges (depending on the desired acceleration potential), which are then picked up by the fast-moving belt and discharged on the conducting sphere. This leads to charge accumulation in the sphere, and the creation of a

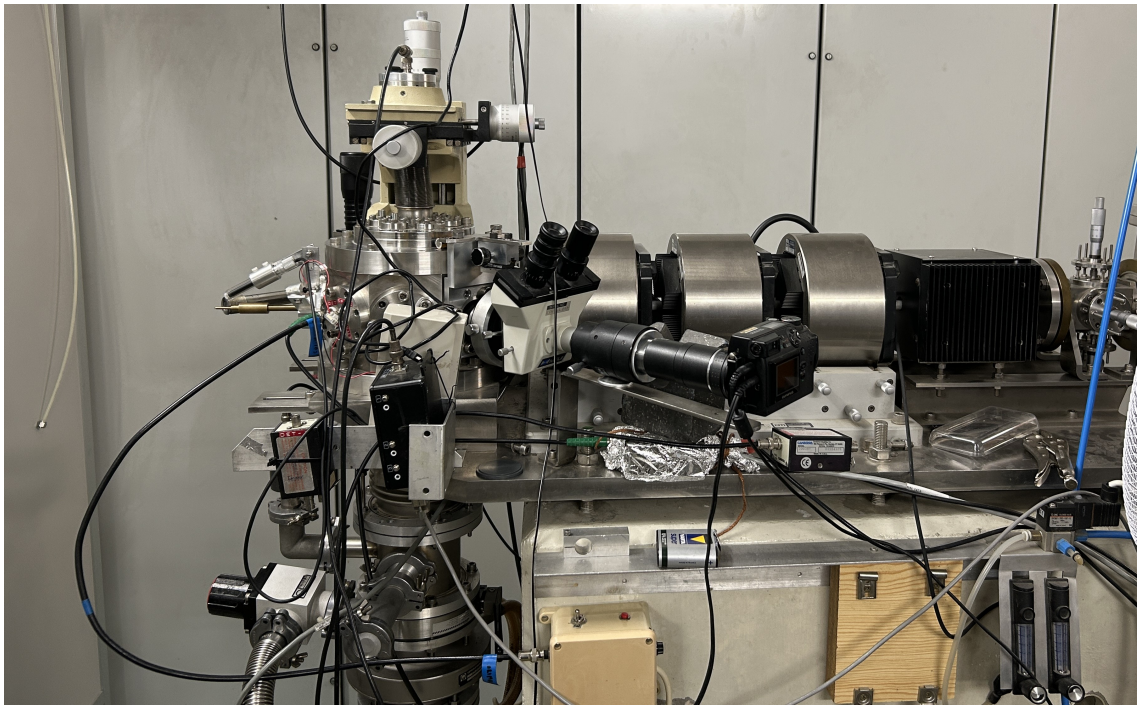

Figure 4.3: Exterior view of the nuclear microprobe reaction chamber.

potential of up to a few million volts.

The charged particles that will originate the beam, protons in this case, are created by an ion source and accelerated by their interaction with the potential accumulated in the above described conducting sphere. A set of beam guidance and optimization devices leads the MeV protons through to the nuclear microprobe reaction chamber, where samples are placed.

4.2.1 Nuclear Microprobe

The nuclear microprobe was added to the Van de Graaff setup in 1999 [36] (figure 4.3), and grants the possibility of doing internal, in-vacuum measurement as well as external beam measurements. The latter, although relevant for the analysis of larger samples, was not used for phosphogypsum samples.

The setup is based on the OM150 from Oxford Microbeams and allows the beam to be focused down to an area of $3 \times 4\ \mu m^2$, offering exceptional spatial resolution. Furthermore, the beam can be set to sweep the sample and create a $2640 \times 2640\ \mu m^2$ elemental composition map. These scans are a very useful tool for assessing sample homogeneity and element dispersion.

X-rays are detected using a Silicon Drift Detector (SDD) and scattered particles are detected in the chamber using a system similar to the one installed in the NRA chamber, and described in subsection 4.1.2.

4.3 Sample Preparation and Measurement

As previously described, phosphogypsum is a granular powder. This is not ideal for analysis. For this reason, the powder was compressed into homogenous pellets, which can then be placed inside the reaction chambers, in the sample holder (figure 4.4). These were pumped to a vacuum of around 10^{-6} mbar and the beam parameters were optimized. The duration of measurements varied quite significantly, with different techniques and conditions of the beam. Nonetheless, measurement time was always managed, in order to obtain data with statistical relevance. The data was converted by 1024 and 8192 channel Analogue to Digital Converter (ADC) and shown in a spectra of counts as a function of channel. A channel to energy conversion is then made, based on a linear adjustment, using two points of known energy, in order to facilitate peak identification.

(a) Sample holder (b) PG pellets

Figure 4.4: Loaded sample holder and compressed PG pellets.

CHAPTER 5

ANALYSIS OF SAMPLE COMPOSITION

A complete and accurate analysis is crucial, to ensure a proper evaluation of each sample's contaminant levels and treatment response. This comprises a set of steps, and interchangeable use of all available methods, as will be presented in this chapter.

It should be noted that, though the employed techniques allow for quantification of almost all elements expected to be found in a PG sample, the analysis was optimized for the ones deemed most important. The selection is based on the economic value and toxicity of each element. To the point, fluorine and REE were given particular significance.

A total of seventeen samples were analysed. These were sent from Germany and France, by other PG2CRM project members.

5.1 Elemental Matrix and Charge Collection

The first step of an accurate analysis is to obtain the elemental matrix of a sample, and the charge collected in its measurement. Though EBS is particularly suited to evaluate depth profile, it is also a valuable tool to start off this assessment.

Figure 5.1 shows the EBS spectrum of one of the analysed samples (L1g). The red triangles represent the experimental points, while the blue line shows a well fitted simulation, done using the NDF software [37]. The procedures within this software are detailed in subsection 5.1.1.

The cutoff in experimental points, observed below channel 50, is purely electronic and has no impact on the results, since no element's scattering energy will be that low. Several barriers (seen as rises in scattered proton counts) can be observed. Their position in the horizontal axis, pertaining to channel or, equivalently, to energy, differs between chemical elements. Taking into account the mechanisms described in section 3.2, this is due to the variation in kinematic factor values, from one element to another. Going back to equation 3.3, we can see that, for the same projectile particle, the kinematic factor increases with an increasing target mass. This can be observed in the spectrum,

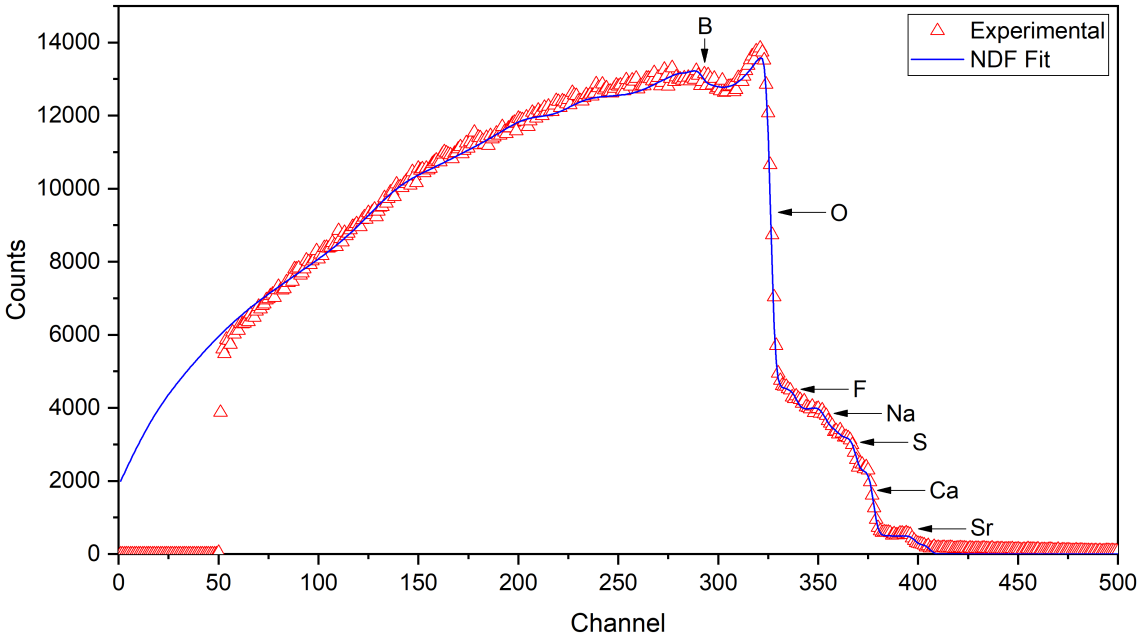

Figure 5.1: EBS spectrum of sample L1g, with main scattering barriers identified.

with lighter elements like boron and oxygen being the furthest to the left, while heavy elements, such as strontium, are further to the right.

The height of said barriers, seen as scattered proton counts, in the vertical axis, is proportional to the quantity of the respective element. As energy decreases, counts from different elements start to superimpose. This must be taken into account when adjusting the spectra. It is also possible to do element quantification, based on the height of the barriers. However, the results obtained through PIGE, for lighter elements, and PIXE, for heavier elements, are more accurate, given the higher sensitivity of these two techniques. Thus, quantification made using EBS is not essential for evaluating the obtained results and will only be presented in appendix A.

Considering that samples are pellets compressed from PG powder, it is fair to say that they are reasonably homogeneous. As such, no shift in barrier energy, derived from energy losses while travelling through the material, will be present. This assumption was confirmed throughout the EBS spectra analysis. Minor non-homogeneous clusters, no larger than a few tenths of a millimetre, seen using the nuclear microprobe, will later be presented. Nonetheless, these are sparse, and their small size makes them mostly irrelevant for the EBS study.

Another crucial information given by the EBS analysis is the charge collected during measurements. The greater the acquisition time the more scattered particles will reach the detector, increasing the number of counts and altering the spectra. A precise collected charge value will help obtain good results when analysing gamma spectra later on.

5.1.1 Spectra Simulation with NDF

Using the NDF software for EBS spectra adjustment relies on 5 main files: a .spc batch file, containing collected charge information and the paths to other necessary files; a .geo file, defining

collision and experimental setup parameters; a .str, defining the samples elemental matrix; a .prf, which adjusts the mass fraction of each of the elements defined in the .str, as well as the number of layers to consider. Given the sample's homogenous nature, a single layer approach was used.

The setup parameters were kept constant for all the samples. A proton beam with approximately 2460 keV and a scattering angle of 155° into a 25 keV resolution PIPS detector. Both the structure and mass fraction files started with an initial guess of sample composition and were adjusted so that the simulated spectra approximated the experimental data points. The collected charge value was adjusted in order to achieve better compatibility between experimental and simulated data.

5.1.2 Excitation Function Calculations

As mentioned in section 3.2, the scattering cross-sections for the collisions considered in these experiments deviate from the Rutherford cross-section calculations. For that reason, previously published cross-section data was used to account for these deviations and ensure proper analysis.

During the course of this work, a few discrepancies were encountered between experimental and simulated data. These were initially attributed to inaccurate cross-section values, particularly for sodium. In an attempt to improve the results and ensure that the used sodium excitation function was reasonable, data previously gathered at the LATR was analysed.

Close to 400 data points, from collisions between protons and two-layered NaF (0.502 Na + 0.498 F) and Ag targets, at energies ranging from approximately 2 to 4 MeV at 157°, were available. Given the high mass of silver atoms, the scattering cross-section for the interaction between these and protons is well described by the Rutherford cross-section. The yield of scattered protons, N_{Ag}, can be expressed as a function of the number of incident protons, N_{protons}, the collision's cross-section, $\sigma^{\mathrm{Ag}}_{\mathrm{Ruth.}}$, target composition, n_{Ag}, and the detectors solid angle and efficiency (equation 5.1). The same can be applied when calculating the scattering yield for sodium (equation 5.2), with the exception of the cross-section values (non-Rutherford).

$$N_{\mathrm{Ag}} = N_{\mathrm{protons}} \sigma^{\mathrm{Ag}}_{\mathrm{Ruth.}} n_{\mathrm{Ag}} \Delta\Omega \varepsilon_{\mathrm{int}} \tag{5.1}$$

$$N_{23\mathrm{Na}} = N_{\mathrm{protons}} \sigma^{23\mathrm{Na}}_{\mathrm{pp}} n_{23\mathrm{Na}} \Delta\Omega \varepsilon_{\mathrm{int}} \tag{5.2}$$

Dividing the two equations, 5.1 and 5.2, we get equation 5.3. This means that the elastic collision cross-section for ^{23}Na can be calculated, if one has information about sample composition and experimental yield, given by the respective peak areas in the obtained spectra.

$$\sigma_{23\mathrm{Na}} = \sigma_{\mathrm{Ag}} \frac{N_{23\mathrm{Na}} n_{\mathrm{Ag}}}{N_{\mathrm{Ag}} n_{23\mathrm{Na}}} \tag{5.3}$$

Given the very large set of points, individually analysing each one quickly became a very time-consuming effort. To avoid this, a Python program was written from scratch, that could automatically open each of the sample's acquired information and compile all results, yielding the complete excitation function of sodium when finished.

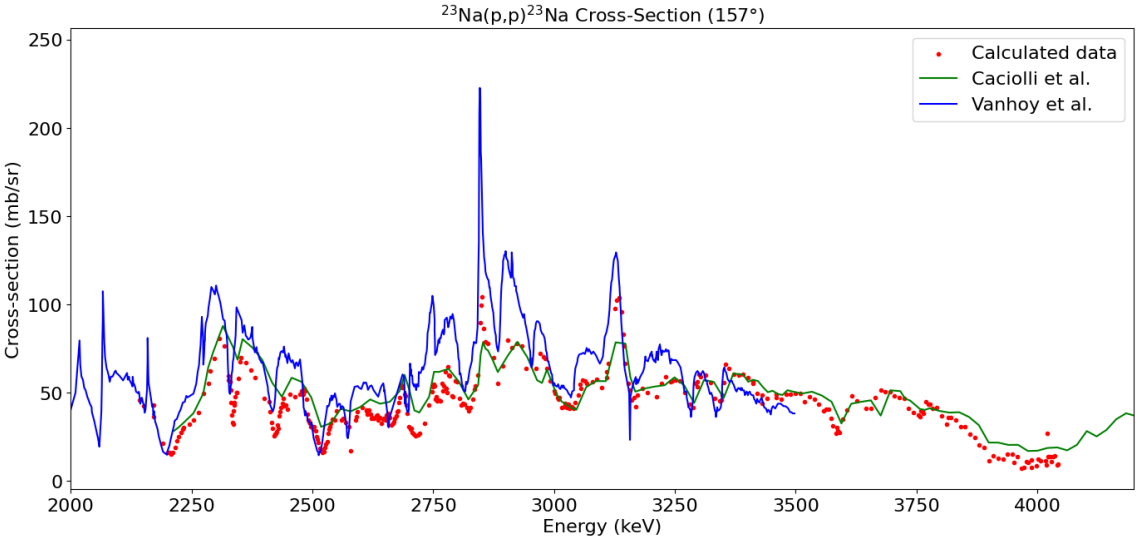

Figure 5.2: Obtained ^{23}Na excitation function for energies between 2 and 4 MeV compared to results published by other authors [38, 39].

The program starts by opening the spectrum of the first sample and identifying the relevant peaks. It then measures the area of the Ag peak. Calculating the area of the Na peak is trickier, as it is partially superimposed with other nuclear reaction's peaks and with background counts. To solve this, the background is first removed, and a Gaussian function is fitted to all peaks adjacent to the Na peak. The area of the relevant Gaussian is then used for subsequent calculations. The same process is sequentially applied to all samples.

Figure 5.2 presents the ^{23}Na(p,p)^{23}Na excitation function obtained in this work, superimposed on previously published data by Caciolli et al. [38] and Vanhoy et al. [39]. Considering the agreement between the newly obtained results and the previously used publications, there was no need to re-analyse the EBS data with a new excitation function.

The program is prepared to apply the same process and calculate other element's excitation functions with just minor tweaks. A few successful tests were conducted for obtaining fluorine cross-section values. This, however, falls outside the scope of this dissertation.

The lack of uncertainty values, for the presented data points, stems from the fact that this work was not originally expected to be part of this dissertation. However, it is currently being worked on and should be available for publication soon.

5.2 Light Element Quantification

Having calculated the elemental matrix and charge collected during measurement, all requirements are met to perform a precise light element analysis, using PIGE. Figure 5.3 presents the gamma spectrum obtained for one of the analysed samples, as an example. Numerous peaks, indicative of gamma emissions and other phenomena, such as electron-positron pair production, Compton scattering or background radiation, may be observed. Similarly to what was described for the EBS spectra, each peaks position in the horizontal energy axis, allows for the identification of a given

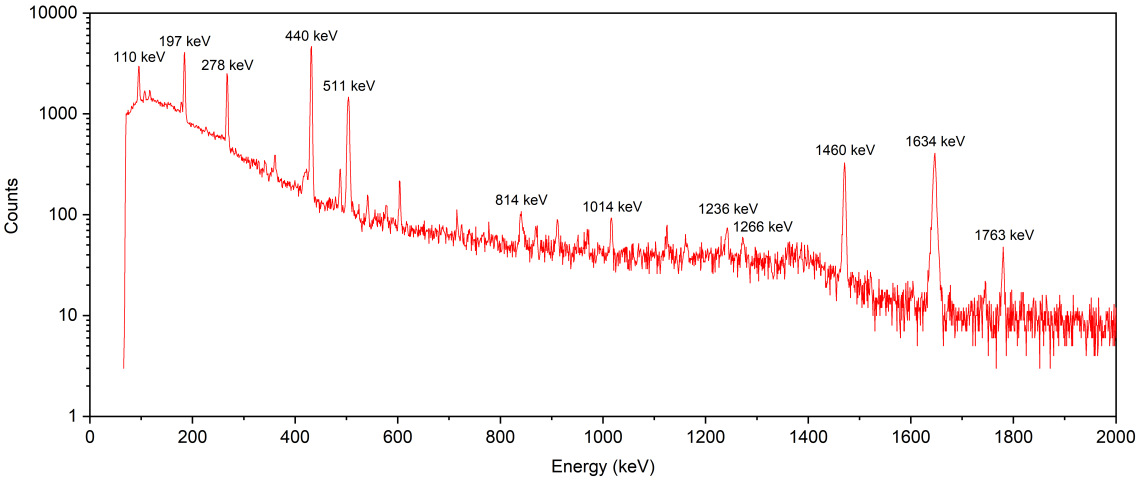

Figure 5.3: PIGE spectrum of sample L1g.

nuclear reaction and, consequently, the nuclei involved. The number of counts, in the vertical axis, expresses a reactions intensity, which is indicative of the relative presence the element in the composition of the sample.

Gamma quantification relies on the ERYA-Bulk software [40], that calculates relative elemental concentrations, given a number of initial parameters: the elemental matrix, an initial guess of each element's concentration, collected charge, proton beam energy and the yield of the observed gamma peaks. The gamma yield was obtained by manually identifying and delimiting each peak, and letting the acquisition program calculate the area of the selected region of interest (ROI). Running the simulation will warrant the mass fraction of each of the elements defined in the sample matrix. For those whose gamma peaks were observed in the spectrum, a theoretical area value will be presented, which allows for simulation accuracy verification, as one can compare the given value with the previously obtained experimental yield.

As expected, this technique shows high sensitivity in the detection of light elements, particularly important in this study, for elements such as fluorine, sodium and aluminium. Table 5.1 shows the main nuclear reactions responsible for the gamma emissions observed not only in the presented spectrum, but throughout the majority of the samples.

Table 5.1: Most relevant gamma spectrum nuclear reactions for sample L1g.

Nuclear Reaction	γ Energy (keV)	Nuclear Reaction	γ Energy (keV)
^{19}F(p,pγ_1)^{19}F	110	^{27}Al(p,pγ_2)^{27}Al	1014
^{19}F(p,pγ_2)^{19}F	197	^{19}F(p,pγ_3)^{19}F	1236
^{198}Au(p,pγ)^{198}Au	278	^{31}P(p,pγ_1)^{31}P	1266
^{23}Na(p,pγ_1)^{23}Na	440	^{23}Na(p,pγ_2)^{23}Na	1634
^{27}Al(p,pγ_1)^{27}Al	814	^{35}Cl(p,pγ_1)^{35}Cl	1763

It is relevant to point out that gold, while having a prominent peak at around 278 keV, is not present in appreciable quantities in any of the analysed samples. Its presence is due to it being the material used in the beam collimators, which are hit by incoming high energy protons, with some

of the radiation from the generated nuclear reaction reaching the detector. The peak seen around 511 keV can be attributed to electron-positron pair annihilation. The large peak at 1460 keV is emitted during beta decay of potassium-40 (^{40}K) to argon-40 (^{40}Ar).

The previous table 5.1 lists only the most common peaks, found across almost all samples, even though with widely varying intensities. It is worth highlighting some other less prominent peaks that were found and taken into account when analysing the results. Examples include: a lithium-7 (^{7}Li) peak at 478 keV; boron-10 (^{10}B) peaks, at 429 keV and 718 keV; a silicon-28 (^{28}Si) peak, at 1779 keV; low intensity gadolinium-157 (^{157}Gd) peaks, at 120 keV and 129 keV.

The absence of elements like oxygen, calcium or sulphur, all major elements in phosphogypsum composition should be noted. For oxygen, particularly, the lack of nuclear reactions with high energy gamma emissions, makes it almost undetectable. For the other two, the number of generated counts is highly diminished, due to the very low gamma emission cross-sections for these elements. For that reason, the subsequently described PIXE analysis is indispensable.

5.3 Heavy Element Quantification

As aforementioned, a PIXE analysis is important for the complete assessment of sample composition, given its ability to accurately quantify elements of high atomic number, an area where PIGE lacks. Furthermore, as atomic number increases, kinematic factor values for neighbouring elements tend to be nearly identical. This hinders chemical element identification through EBS, as the barriers observed in the spectra may be superimposed. Therefore, PIXE also serves as confirmation for the elemental matrix, initially obtained using backscattered protons analysis. It was, in fact, the case that PIXE results revealed some discrepancies in the elemental matrix. As such, EBS and PIGE analyses were redone to ensure sample composition accuracy and rectify any misidentifications.

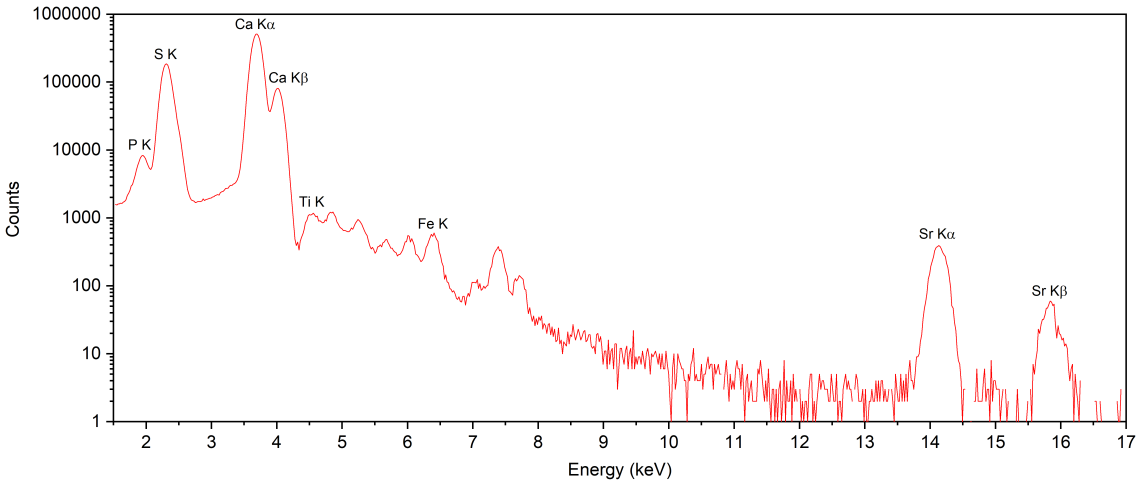

Figure 5.4: PIXE spectrum of sample PgP, at 2020 keV beam energy.

Figure 5.4 shows a PIXE spectrum, obtained for sample PgP, with a beam energy of 2020 keV. A clear presence of elements such as sulphur and calcium was expected, with these two yielding the most intense x-ray emission peaks. Another element that shows a strong presence is strontium,

with both Kα and Kβ peaks visible. This, as will be seen in section 5.4, is common throughout all samples. Other less intense emissions include potassium, titanium and iron.

X-ray yield was calculated using the GUPIXWIN software [41]. It works by providing the program with setup and sample composition parameters and running a simulation, that yields both the experimentally obtained data points and a spectrum, generated based on the inputted parameters. Examining the differences between the experimental data and the simulation and noting the energy at which they are most noticeable, it is possible to correct or input new elements, in order to match the simulation to the experimental data points. After achieving good agreement between them, the program will output a relative concentration for each of the sample's constituent.

All samples were subjected to a second PIXE analysis, varying beam energy from 2020 keV to around 700 keV. The spectrum for the same sample, PgP, is now shown for a 700 keV beam energy, in figure 5.5. The shift towards lower energies facilitates the detection of lighter elements, whose x-ray emission cross-sections are higher in this range. Moreover, given the high energy scattered protons, present at 2020 keV, a protective Mylar filter has to be put in front of the x-ray detector, preventing lower energy x-rays from reaching it. This filter in not used for analysis with a 700 keV beam energy, allowing all radiation to reach the detector.

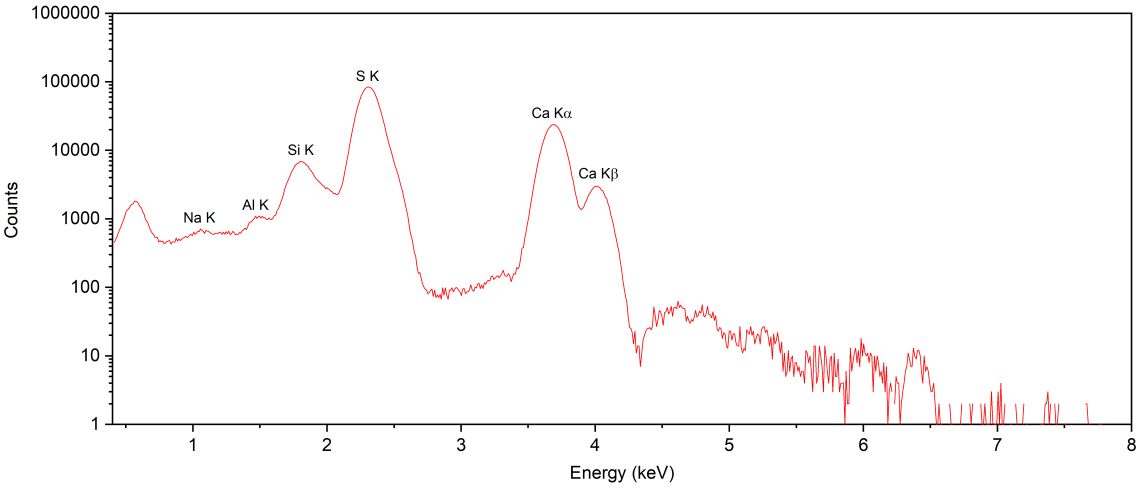

Figure 5.5: PIXE spectrum of sample PgP, at 700 keV beam energy.

Comparing both spectra, and the peaks identified in each one, it is clear that elements above calcium are significantly attenuated in the lower energy spectrum, as expected. Heavier elements, such as titanium, iron and specially strontium, are barely noticeable in this spectrum, being, however, easily detected in the 2020 keV spectrum. Furthermore, the 700 keV spectrum shows lighter element emissions, for example, sodium, aluminium, silicon and phosphorus, which are masked in the higher energy spectrum. These conclusions can be extended to all samples in this study.

5.3.1 Elemental mapping

As referred to, in subsection 4.2.1, the nuclear microprobe has the capability of performing area scans. With these scans, elemental distribution maps for the selected area of a sample can be

performed. Figure 5.6 shows the distribution of four of the identified elements, in sample L1g.

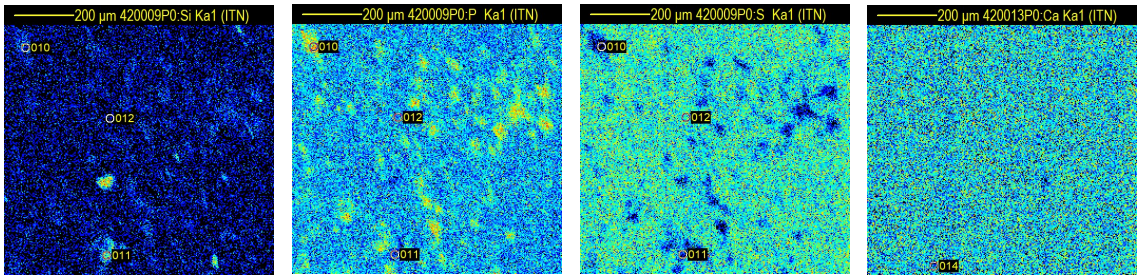

(a) Silicon (b) Phosphorus (c) Sulphur (d) Calcium

Figure 5.6: Maps of elemental distribution obtained with the nuclear microprobe, for sample L1g.

The four elemental distribution maps reveal that the samples exhibit a predominantly homogeneous composition. This is particularly true for calcium, one of phosphogypsum's main constituents. Other elements, such as silicon, phosphorus and sulphur show noticeable hotspots. There also appears to be a link between sulphur and phosphorus with areas lacking the former having a higher concentration of the latter. Despite the few hotspots, evident in the elemental distribution, and relationships that may be established between the concentrations in these areas, they are relatively small and do not significantly interfere with the overall homogeneous nature of the samples.

These hotspots could, however, justify some of the issues encountered when analysing EBS data, which ultimately led to the work described in subsection 5.1.2.

5.4 Comparative Analysis of All Acquired Data

Tables 5.2, 5.3 and 5.4 display the chemical composition of all samples. As expected, a wide variation in the sample's composition was observed, due to different originating phosphate rocks, as well as treatments later applied to the phosphogypsum.

Fluorine stands out as the most important element within the scope of this work, both due to its high toxicity and the difficulty in detecting it through other techniques. The use of PIGE provides high sensitivity for fluorine detection, making it essential for a complete characterization of phosphogypsum's environmental hazards and possible efficiency of fluorine removal treatments. Fluorine concentration values range from 0.003 wt.% in sample L3BS, to as high as 0.691 wt.% in sample W1DS. Even the lowest value can pose an environmental risk. The gypsum industry specifies a value of 200 mg/kg of fluoride for the recycling or disposal of phosphogypsum waste and a limit as low as 10 mg/kg for use in rotary kilns, when performing gypsum calcination. In addition, according to the World Health Organization, the maximum allowable fluorine concentration in water is 1.5 mg/kg. This suggests that water coming into contact with phosphogypsum, with fluorine concentrations similar to those presented here, could leach unsafe amounts of this element, even if leaching efficiency is relatively low.

It is important to address the fact that the PIGE data is presented without uncertainty values. These come from a variety of places, such as cross-section and solid angle variations as well

as ERYA's own adjustment uncertainty. As of the time of writing, ERYA does not provide the uncertainty value associated with its adjustment and, for that reason, the overall uncertainty values could not be calculated properly. The tables containing PIXE data are here presented without the associated uncertainties for better readability. A complete version, listing the fitting error for each of the presented values can be found in appendix A.

It is also clear that calcium and sulphur keep a constant, high concentration throughout all samples, with values ranging from 19.4% to 23.8%, for sulphur, and 26% to 29%, for calcium. Oxygen also fits in this category although being, for reasons previously stated, impossible to accurately quantify via the used techniques. Other elements, such as aluminium, silicon, titanium, iron and strontium, are constantly present in low concentration, which is typical for geological materials originating from sedimentary or igneous phosphate rocks.

A few outlier values can be identified. For example, a high phosphorus concentration in the Moroccan sample, high chlorine concentration in sample NRTCa, high silicon concentration in sample L3D or high sodium concentration in sample Na4O-4-70. These rare high concentration instances are probably justified by the chemical compounds that come in contact with the PG, when these are undergoing decontamination or element extraction.

While different techniques provide slightly varying quantifications for the same elements, these discrepancies do not significantly impact the overall conclusions of this study. These discrepancies arise from the different cross sections associated with varying beam energies, as well as the inherent uncertainties in each technique and slight heterogeneity of the samples, as referenced earlier.

Lastly, as seen from the data above, REE detection was not particularly strong, with only trace amounts of cerium and gadolinium identified in a few samples. Although this could mean that the samples in this study were poor in REE concentration, there is a high probability that more of these materials could be detected, given a more adequate setup. The used setup's limitation stems from the inadequacy of PIGE for detecting heavier elements, as noted in section 3.5. In the case of PIXE, the available setup was not capable of adequately detecting x-rays above approximately 30 keV, where most REE x-ray emissions occur, due to a significant drop in detector efficiency beyond this threshold. In the future, a new detector is expected to be integrated into the current setup to enable the quantification of elements emitting in higher energy ranges. However, due to the reasons outlined above, this was not feasible during the development of this study and, as such, will not be further explored.

Table 5.2: Elemental composition of all analysed samples, obtained using PIGE.

Sample	Concentration (wt.%)					
	Boron	Fluorine	Sodium	Aluminium	Silicon	Phosphorus
L1g	0.169	0.063	0.160	0.179	0.000	0.164
Dg1	0.102	0.047	0.051	1.226	1.809	0.000
Pg1B	0.196	0.235	0.054	0.070	0.763	0.000
PgP	0.000	0.623	0.052	0.080	0.000	0.000
L3D	0.181	0.063	0.062	0.136	4.976	0.000
NRTCa	0.905	0.290	0.076	0.077	0.216	0.000
L3BS	0.204	0.031	0.069	0.154	0.000	0.346
W1DS	0.122	0.691	0.083	0.110	0.000	0.176
Na4O-4-70	0.054	0.166	9.019	0.221	0.000	0.851
L1FS	0.001	0.066	0.091	0.756	0.000	0.353
W1CS	0.000	0.283	1.326	0.157	0.000	0.224
W2BS	0.002	0.280	3.058	0.103	0.000	0.718
NH4-RH-24	0.000	0.218	0.104	0.219	0.000	0.133
SAIS	0.000	0.112	0.037	0.036	0.000	0.078
M54	0.000	0.003	0.097	0.249	0.000	0.503
PGP	0.000	0.350	0.032	0.135	0.000	0.159
Moroccan	0.000	0.457	0.273	0.090	0.000	2.675

Table 5.3: Elemental composition of all analysed samples, obtained using PIXE, with 2020 keV beam energy.

Sample	Concentration (wt.%) (normalized to 100%)									
	Silicon	Phosphorus	Sulphur	Chlorine	Calcium	Titanium	Iron	Strontium	Cerium	Gadolinium
L1g	0.165	0.000	23.486	0.071	26.997	0.072	0.526	1.840	0.112	0.010
Dg1	0.611	0.000	23.385	0.069	28.549	0.003	0.045	0.172	0.000	0.008
Pg1B	0.378	0.000	22.840	0.067	28.398	0.055	0.034	1.718	0.123	0.006
PgP	0.000	0.000	23.163	0.097	28.022	0.060	0.064	1.856	0.219	0.022
L3D	0.302	0.000	23.398	0.097	27.406	0.027	0.081	1.803	0.091	0.000
NRTCa	0.037	0.000	21.946	6.023	27.067	0.035	0.047	0.803	0.112	0.007
SAIS	0.549	0.000	22.367	0.076	28.648	0.046	0.067	2.173	0.042	0.000
M54	0.108	0.194	23.855	0.063	27.142	0.012	1.215	0.075	0.003	0.000
PGP	0.339	0.000	22.254	0.091	29.036	0.086	0.078	2.008	0.245	0.012
Moroccan	0.000	6.229	19.432	0.046	26.375	0.015	0.095	0.076	0.000	0.010

Table 5.4: Elemental composition of all analysed samples, obtained using PIXE, with 700 keV beam energy.

Sample	Concentration (wt.%) (normalized to 100%)											
	Sodium	Magnesium	Aluminium	Silicon	Phosphorus	Sulphur	Chlorine	Calcium	Titanium	Iron	Strontium	Cerium
L1g	0.129	0.000	0.036	0.233	0.239	23.115	0.067	26.772	0.061	0.594	2.022	0.183
Dg1	0.045	0.564	0.144	0.710	0.000	22.362	0.085	29.207	0.000	0.090	0.237	0.030
Pg1B	0.050	0.007	0.058	0.470	0.171	21.451	0.069	29.714	0.053	0.132	2.099	0.166
PgP	0.069	0.013	0.089	0.322	0.267	22.790	0.080	27.497	0.045	0.103	2.089	0.241
L3D	0.025	0.002	0.013	0.422	0.174	22.980	0.067	27.408	0.020	0.048	2.200	0.108
NRTCa	0.053	0.001	0.030	0.546	0.078	21.685	5.121	26.304	0.035	0.119	1.002	0.105
SAIS	0.039	0.004	0.030	0.444	0.079	22.975	0.066	27.267	0.066	0.021	2.526	0.039
M54	0.132	0.031	0.045	0.434	1.364	23.614	0.057	24.164	0.014	2.105	0.059	0.000
PGP	0.063	0.010	0.135	1.138	0.276	22.235	0.065	27.283	0.078	0.076	1.950	0.244
Moroccan	0.358	0.455	0.123	0.255	7.238	18.544	0.051	24.893	0.012	0.074	0.086	0.000

CHAPTER 6

RADIOLOGICAL RISK ASSESSMENT

As emphasized in chapter 2, one of the main deterrents from phosphogypsum use, in industrial and agricultural settings, is its high radionuclide content. In order to better understand the effects of the use of contaminated PG, gamma spectroscopy was employed to quantify potentially hazardous elements such as uranium, thorium, radium, potassium and lead. This chapter will briefly introduce the most common parameters used to perform radiological risk assessments and evaluate the potential radiological impact of the analysed samples.

6.1 Radionuclide Activities in Building Materials

Phosphogypsum's characteristics, as mentioned in the early chapters of this work, offer a great amount of possible use cases. For that reason, the analysis of the impact of PG in real case scenarios is of paramount importance, both for construction workers and for people who will possibly come in contact with the material.

The most used radionuclides in radiological risk assessment are ^{226}Ra, ^{232}Th and ^{40}K, due to their common presence in geological samples and building materials and high impact in natural radioactivity measurements. As such, we shall focus our analysis on these species. Table 6.1 presents the activities of radionuclides, measured in this work (see subsection 6.1.3.1 for details on the calculation of ^{232}Th activity) and figure 6.1 shows the average activity of each of the aforementioned radionuclides for a variety of different building materials, including regular gypsum.

6.1.1 Radium-226

The analysed phosphogypsum samples have an average ^{226}Ra activity of 211.31 Bq/kg. When comparing this value with other building materials (see figure 6.1(a)) we see that it places PG slightly above the average regular gypsum activity of 140 Bq/kg and only lower than the average activity of granite, at 1037 Bq/kg. Taking a closer look we can see that only 3 of the 10 analysed

Table 6.1: Activity in PG samples, for the most important radionuclides in construction raw materials.

Sample	Activity (Bq/kg)					
	K-40	Ra-226	Ra-228	Pb-210	U-235	Th-232
POL	0.0	35.3	68.9	0.0	0.0	68.9
CRO	79.0	720.0	11.3	939.0	17.0	11.3
HUV	0.0	847.0	11.3	2007.0	0.0	11.3
Na4O-4-70	0.0	21.5	29.0	0.0	0.0	29.0
W1DS	0.0	31.3	56.0	0.0	0.0	56.0
W1CS	0.0	37.0	43.0	0.0	0.0	43.0
W2BS	0.0	32.0	50.0	0.0	0.0	50.0
L3BS	0.0	214.0	0.0	0.0	0.0	0.0
NH4-RT-24	0.0	113.0	51.0	0.0	0.0	51.0
L1FS	0.0	62.0	51.0	0.0	0.0	51.0

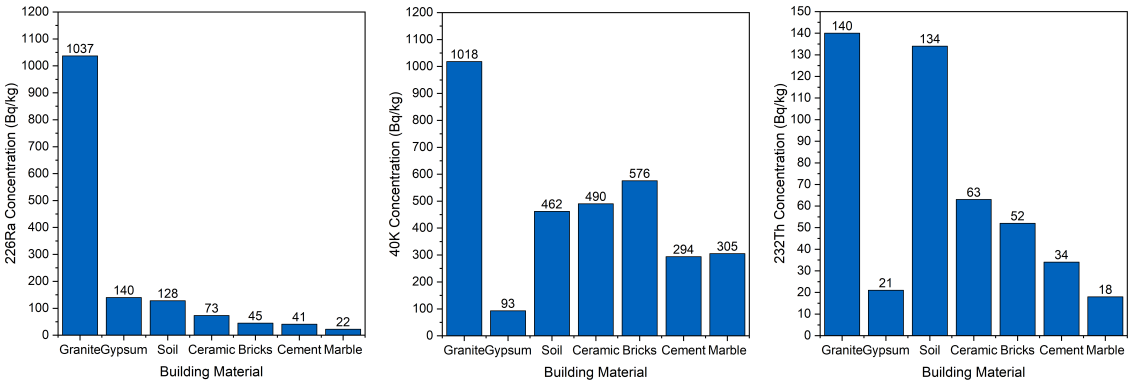

(a) ^{226}Ra (b) ^{40}K (c) ^{232}Th

Figure 6.1: Average activity of ^{226}Ra, ^{40}K and ^{232}Th in building materials. Retrieved from [42].

samples (CRO, HUV, L3BS) have a higher activity that the average for gypsum. Furthermore, only 4 samples present an activity above the established safety limit of 50 Bq/kg [43].

6.1.2 Potassium-40

All but one of the analysed samples had a detectable amount of ^{40}K activity. For the sample with an appreciable activity (CRO), its 79 Bq/kg would place it after granite and soil (see figure 6.1(b)) and very far from the established safety limit of 500 Bq/kg [43], although almost four times higher than the average ^{40}K activity in regular gypsum.

6.1.3 Thorium-232

The analysed phosphogypsum samples have an average ^{232}Th activity of 37.15 Bq/kg. This value would place it below granite, soil, ceramic and bricks in average activity (see figure 6.1(c)). All but 3 samples (CRO, HUV and L3BS) have a higher activity than the average for regular gypsum,

with 5 of the samples (POL, W1DS, W2BS, NH4-RT-24, L1FS) being at or above the established 50 Bq/kg safety limit [43].

6.1.3.1 Estimation of ^{232}Th activity

It should be noted that the activity of ^{232}Th was not measured directly. Instead, since ^{228}Ra is part of the decay series of ^{232}Th, originating from alpha decay of the latter, we can use its activity to estimate the activity of ^{232}Th. The relation between these element's activities depends on various factors. For simplicity, we shall assume that there are no other sources of ^{228}Ra, besides the aforementioned alpha decay. In this case, two possibilities arise: the radioisotopes may or may not have achieved secular equilibrium.

Since the half-life value of ^{228}Ra (approximately 5.75 years) is much shorter than ^{232}Th (approximately 1.405×10^{10} years), it will come a point where the activity of ^{228}Ra can't increase any further, due to the lack of atoms from the ^{232}Th decay. This means that radium activity will be limited by thorium's rate of decay. If so, secular equilibrium has been reached and both radionuclide's activities will be equal.

Due to possible disruption of decay chains, caused by treatments applied to the samples, equilibrium may have been disturbed. Nonetheless, for simplicity, we shall consider that the sample's ^{232}Th and ^{228}Ra quantities have achieved secular equilibrium.

6.2 Parameters for Classification of Building Materials

In order to facilitate the radiological comparison between different building materials and evaluate their adequacy for use in construction, several parameters were introduced by the United Nations Scientific Comitee on the Effects of Atomic Radiation (UNSCEAR) and are frequently employed. These are described in the following subsections and calculated for the samples in this study.

6.2.1 Gamma Index

The Gamma Index is mainly used for the assessment of the level of gamma radiation, emitted from building materials. Is is given by equation 6.1 [42].

$$I_\gamma = \frac{A_{226\mathrm{Ra}}}{300} + \frac{A_{232\mathrm{Th}}}{200} + \frac{A_{40\mathrm{K}}}{3000} \tag{6.1}$$

6.2.2 Radium Equivalent Activity

Another important parameter is Radium equivalent activity ($\mathrm{Ra_{eq}}$), a single value used to represent the overall radioactivity of materials containing a mixture of ^{226}Ra, ^{232}Th, and ^{40}K (see equation 6.2). It exists as a way to simplify radiation hazard assessments by combining their contributions into a single, standardized unit. It is calculated based on the assumption that 1 Bq of^{226}Ra, 0.7 Bq of ^{232}Th, and 13 Bq of ^{40}K produce the same gamma dose rate. The limit for $\mathrm{Ra_{eq}}$ in construction materials is often set at 370 Bq/kg [42].

$$\mathrm{Ra_{eq}} = A_{226\mathrm{Ra}} + 1.43A_{232\mathrm{Th}} + 0.077A_{40\mathrm{K}} \tag{6.2}$$

6.2.3 Hazard Indexes

The External Hazard Index (H_{ex}) is a parameter used to evaluate the potential radiological hazard posed by any Naturally Occurring Radioactive Material (NORM) (see equation 6.3). It is designed to ensure that the radiation dose from these materials does not exceed the safety limit for the general public, as recommended by international radiation protection guidelines. Its value should be less than 1 to ensure that the material is safe for use in construction [43].

$$H_{\mathrm{ex}} = \frac{A_{226\mathrm{Ra}}}{370} + \frac{A_{232\mathrm{Th}}}{259} + \frac{A_{40\mathrm{K}}}{4810} \tag{6.3}$$

Lastly, the Internal Hazard Index (H_{in}), used to evaluate the exposure to products of the aforementioned decay chains, such as ^{222}Rn and its daughter isotopes (see equation 6.4). Similarly to the external hazard index, its value should be below 1, for a material to be considered safe for use [43].

$$H_{\mathrm{in}} = \frac{A_{226\mathrm{Ra}}}{185} + \frac{A_{232\mathrm{Th}}}{259} + \frac{A_{40\mathrm{K}}}{4810} \tag{6.4}$$

6.2.4 Cross-Comparison of Radiological Risk Data

Table 6.2 exhibits the Radium equivalent activity, Gamma Index and Hazard Indexes values for all the analysed samples.

Table 6.2: Radium equivalent activity, Gamma Index and Hazard Indexes for all the analysed samples.

Sample	$\mathrm{Ra_{eq}}$ (Bq/kg)	I_γ	H_{ex}	H_{in}
POL	133.83	0.46	0.36	0.46
CRO	742.24	2.48	2.01	3.95
HUV	863.16	2.88	2.33	4.62
Na4O-4-70	62.97	0.22	0.17	0.23
W1DS	111.38	0.38	0.30	0.39
W1CS	98.49	0.34	0.27	0.37
W2BS	103.50	0.36	0.28	0.37
L3BS	214.00	0.71	0.58	1.16
NH4-RT-24	185.93	0.63	0.50	0.81
L1FS	134.93	0.46	0.36	0.53

Only 2 samples (CRO and HUV) exceed the imposed 370 Bq/kg limit for Radium equivalent activity. Additionally, as previously mentioned, materials with hazard indexes above 1 are not safe for use as a construction material. The same 2 samples present a high value of H_{ex}, while 3 samples (CRO, HUV and L3BS) are above 1 on the H_{in} hazard index and, as such should not be used.

Table 6.3: Comparison of Radium equivalent dose, Gamma Index and Hazard Indexes between the average of the analysed samples and other building materials [42].

Material	Ra_{eq} (Bq/kg)	I_γ	H_{ex}	H_{in}
Sample avg.	**265.04**	**0.89**	**0.72**	**1.29**
Bricks	163.28	0.60	0.44	0.56
Cement	112.53	0.41	0.30	0.42
Soil	328.89	1.16	0.89	1.17
Granite	1350.89	4.61	3.65	6.55
Gypsum	171.43	0.58	0.46	0.84
Marble	65.37	0.28	0.20	0.26
Ceramic	205.23	0.72	0.54	0.73

Table 6.3 presents a comparison between the average value of each of the calculated parameters for all analysed samples and common building materials.

6.3 Radiation Exposure

Quantification of the effects of radiation exposure relies on two main units. The Gray (Gy) is a unit of absorbed radiation dose and represents the amount of energy, from ionizing radiation, that is absorbed per unit mass of a material. One Gray is equal to one joule of energy absorbed per kilogram of matter. On the other hand, the Sievert (Sv) measures the biological effect of radiation, taking into account not just the energy absorbed, as measured by the Gray, but also the type of radiation and its impact on living tissues. This is done by applying a weighting factor to the absorbed dose to reflect the different levels of biological harm caused by various types of radiation.

Within the scope of this study, two scenarios will be considered in the assessment of the potential radiation hazard, when using phosphogypsum based materials. Firstly, we shall calculate the absorbed gamma radiation dose, for each of the previously listed samples, at a height of 1 m above the ground. This is given by equation 6.5, in nGy/h. The recommended safety limit for this index, as reported by UNSCEAR [43], is 84 nGy/h.

$$\mathrm{D} = 0.462 A_{226\mathrm{Ra}} + 0.604 A_{232\mathrm{Th}} + 0.0417 A_{40\mathrm{K}} \tag{6.5}$$

Having calculated this value, we can evaluate the effective dose, received by people either living within or nearby the area of study, built using bricks containing phosphogypsum. Expressions for both scenarios are provided in equations 6.6 and 6.7, respectively, with the AED given in mSv/y.

$$\mathrm{AED}_{\mathrm{indoor}} = \mathrm{D} \times 8760\,\mathrm{h} \times 0.8 \times 0.7 \times 10^{-6} \tag{6.6}$$

$$\mathrm{AED}_{\mathrm{outdoor}} = \mathrm{D} \times 8760\,\mathrm{h} \times 0.2 \times 0.7 \times 10^{-6} \tag{6.7}$$

The maximum acceptable AED for the general public from radiation exposure is 1 mSv/y. This limit is recommended by international organizations, such as the International Commission on

Radiological Protection (ICRP) and the International Atomic Energy Agency (IAEA). This value is set to minimize health risks, such as cancer, which can be caused by higher levels of radiation over time. It is a precautionary measure, as even small increases in exposure above natural levels can contribute to long-term effects. It should be noted that this limit is designed for additional exposure, beyond natural background, including radon, cosmic rays and terrestrial radiation. For people working in radiation related fields, an occupational exposure limit is set at a much higher 20 mSv/y.

Table 6.4 sums up the data collected for both exposure scenarios, as well as the more comprehensive absorbed dose values.

Table 6.4: Absorbed doses and annual effective doses for different exposure conditions.

Sample	D (nGy/h)	AED_{indoor} (mSv/y)	$AED_{outdoor}$ (mSv/y)
POL	57.92	0.28	0.07
CRO	342.76	1.68	0.42
HUV	398.14	1.95	0.49
Na4O-4-70	27.45	0.13	0.03
W1DS	48.28	0.24	0.06
W1CS	43.07	0.21	0.05
W2BS	44.98	0.22	0.06
L3BS	98.87	0.49	0.12
NH4-RT-24	83.01	0.41	0.10
L1FS	59.45	0.29	0.07

These values are representative of samples of different origin, that undergone a variety of treatments which could have led to significant alterations in their radionuclide concentrations. Nonetheless, most samples are within the annual exposure limits, with only CRO and HUV surpassing 1 mSv/y when evaluated for a person living inside a structure built with those materials.

CHAPTER 7

CONCLUSIONS

This study sought to analyse the chemical composition of phosphogypsum samples, as part of the PG2CRM collaboration, focusing on their fluorine, radioactive material and REE content. For that purpose IBA techniques, namely PIGE, PIXE and EBS, were employed, as they allowed for complete sample characterization with very high sensitivity especially for light elements like fluorine, whose quantification through other techniques is subpar.

Chemical composition data showed constant high concentrations of the main constituents of the gypsum phase, calcium and sulphur, as well as a multitude of other minor elements, such as sodium, phosphorus, silicon, titanium, iron and strontium. More importantly, an accurate quantification of fluorine was achieved, with concentrations ranging from 0.003% to 0.691%, proving that treatments have to be applied to PG to assure fluorine removal, as the obtained values were too high for use in the gypsum industry and posed a health and environmental risk. An improvement to be made is the incorporation of a more reliable REE detection setup, given that only low cerium and gadolinium concentrations were observed. It could be the case that the analysed samples had low REE presence, but there were known limitations in the utilized setup that should be corrected to ensure the most accurate analysis possible.

Radiological composition data was limited and should be expanded in future works, to allow for a more complete assessment. Nevertheless, a thorough analysis of the available data demonstrated that most of the samples in this study were low in radiological hazard, scoring below the imposed limits in almost all radiological evaluation parameters. Only two samples had enough radionuclide activity to pose danger if used as a construction material. The lack of these radioactive species could possibly be attributed to the treatments previously applied to the samples.

With nothing more to add, we look to the future hoping that progress is made, in order to improve the percentage of recycled PG, not only as a means to mitigate the environmental burden posed by current large-scale stockpiling, but also as this material holds promise to fill the expected gypsum gap.

Bibliography

[1] J. M. Lourenço. *The NOVAthesis LaTeX Template User's Manual*. NOVA University Lisbon. 2021. URL: https://github.com/joaomlourenco/novathesis/raw/main/template.pdf (cit. on p. i).

[2] N. Haneklaus et al. "Closing the upcoming EU gypsum gap with phosphogypsum". In: *Resources, Conservation and Recycling* 182 (2022-07). ISSN: 18790658. DOI: 10.1016/j.resconrec.2022.106328 (cit. on pp. 1, 4).

[3] H. Tayibi et al. "Environmental impact and management of phosphogypsum". In: *Journal of Environmental Management* 90 (8 2009), pp. 2377–2386. ISSN: 03014797. DOI: 10.1016/j.jenvman.2009.03.007 (cit. on pp. 3, 4, 6).

[4] L. Maina et al. "Chemical and radiochemical characterization of phosphogypsum from Poland". In: *Nukleonika* 69 (2 2024-06), pp. 113–117. ISSN: 15085791. DOI: 10.2478/nuka-2024-0016 (cit. on pp. 3, 4).

[5] N. H. Koralegedara et al. "Recent advances in flue gas desulfurization gypsum processes and applications – A review". In: *Journal of Environmental Management* 251 (2019-12). ISSN: 10958630. DOI: 10.1016/j.jenvman.2019.109572 (cit. on p. 4).

[6] K. Layr and P. Hartlieb. "Market Analysis for Urban Mining of Phosphogypsum". In: *BHM Berg- und Hüttenmännische Monatshefte* 164 (6 2019-06), pp. 245–249. ISSN: 0005-8912. DOI: 10.1007/s00501-019-0855-8 (cit. on p. 4).

[7] A. Gaudry et al. "Heavy metals pollution of the atlantic marine environment by the Moroccan phosphate industry, as observed through their bioaccumulation in Ulva lactuca". In: *Water, Air, and Soil Pollution* 178 (1-4 2007), pp. 267–285. ISSN: 15732932. DOI: 10.1007/s11270-006-9196-9 (cit. on p. 5).

[8] World Health Organization. *Guidelines for drinking-water quality: Fourth edition incorporating the first and second addenda*. Geneva, Switzerland, 2022. ISBN: 978-92-4-004506-4 (cit. on p. 5).

[9] S. Sahu et al. "Natural radioactivity assessment of a phosphate fertilizer plant area". In: *Journal of Radiation Research and Applied Sciences* 7 (1 2014-01), pp. 123–128. ISSN: 16878507. DOI: 10.1016/j.jrras.2014.01.001 (cit. on p. 5).

[10] United States Environmental Protection Agency. *Radioactive Decay*. https://www.epa.gov/radiation/radioactive-decay. Accessed: September, 2024 (cit. on p. 6).

[11] F. Papageorgiou et al. "Environmental impact of phosphogypsum stockpile in remediated Schistos waste site (Piraeus, Greece) using a combination of gamma-ray spectrometry with geographic information systems". In: *Environmental Monitoring and Assessment* 188 (3 2016-03), pp. 1–14. ISSN: 15732959. DOI: 10.1007/s10661-016-5136-3 (cit. on p. 6).

[12] M. J. Madruga et al. "Distribution of Natural Radionuclides, Rare Earth Elements, Metals and Metalloids in a Phosphogypsum Stockpile". In: *International Journal of Waste Resources* 09 (01 2019). DOI: 10.35248/2252-5211.19.9.363 (cit. on p. 6).

[13] S. M. Luther, M. J. Dudas, and P. M. Rutherford. "Radioactivity and Chemical Characteristics of Alberta Phosphogypsum". In: *Water, Air and Soil Pollution* 69 (1993-07), pp. 277–290. DOI: 10.1007/BF00478164 (cit. on p. 6).

[14] J. M. Abril, R. García-Tenorio, and G. Manjón. "Extensive radioactive characterization of a phosphogypsum stack in SW Spain: 226Ra, 238U, 210Po concentrations and 222Rn exhalation rate". In: *Journal of Hazardous Materials* 164 (2-3 2009-05), pp. 790–797. ISSN: 03043894. DOI: 10.1016/j.jhazmat.2008.08.078 (cit. on p. 6).

[15] B. Mazzilli et al. "Radiochemical characterization of Brazilian phosphogypsum". In: *Journal of Environmental Radioactivity* 49.1 (2000), pp. 113–122. ISSN: 0265-931X. DOI: 10.1016/S0265-931X(99)00097-1 (cit. on p. 6).

[16] M. Olszewska-Wasiolek. "Estimates of the Occupational Radiological Hazard in the Phosphate Fertilizers Industry in Poland". In: *Radiation Protection Dosimetry* 58.4 (1995-03), pp. 269–276. ISSN: 0144-8420. DOI: 10.1093/oxfordjournals.rpd.a082624 (cit. on p. 6).

[17] L. A. Attar et al. "Radiological impacts of phosphogypsum". In: *Journal of Environmental Management* 92 (9 2011), pp. 2151–2158. ISSN: 10958630. DOI: 10.1016/j.jenvman.2011.03.041 (cit. on p. 6).

[18] N. K. Ahmed. "Measurement of natural radioactivity in building materials in Qena city, Upper Egypt". In: *Journal of Environmental Radioactivity* 83 (1 2005), pp. 91–99. ISSN: 0265931X. DOI: 10.1016/j.jenvrad.2005.03.002 (cit. on p. 6).

[19] R. Pérez-López, A. M. Álvarez Valero, and J. M. Nieto. "Changes in mobility of toxic elements during the production of phosphoric acid in the fertilizer industry of Huelva (SW Spain) and environmental impact of phosphogypsum wastes". In: *Journal of Hazardous Materials* 148 (3 2007-09), pp. 745–750. ISSN: 03043894. DOI: 10.1016/j.jhazmat.2007.06.068 (cit. on p. 7).

[20] J. P. Bolivar, R. Garcia-Tenorio, and F. Vaca. "Radioecological Study of an Estuarine System Located in the South of Spain". In: *Water Research* 34 (11 2000-08), pp. 2941–2950. ISSN: 0043-1354. DOI: 10.1016/S0043-1354(99)00370-X (cit. on p. 7).

[21] Y. Chernysh et al. "Phosphogypsum recycling: A review of environmental issues, current trends, and prospects". In: *Applied Sciences (Switzerland)* 11 (4 2021-02), pp. 1–22. ISSN: 20763417. DOI: 10.3390/app11041575 (cit. on p. 7).

[22] X. Qin et al. "Resource utilization and development of phosphogypsum-based materials in civil engineering". In: *Journal of Cleaner Production* 387 (2023-02). ISSN: 09596526. DOI: 10.1016/j.jclepro.2023.135858 (cit. on p. 7).

[23] A. A. Cuadri et al. "Valorization of phosphogypsum waste as asphaltic bitumen modifier". In: *Journal of Hazardous Materials* 279 (2014-08), pp. 11–16. ISSN: 18733336. DOI: 10.1016/j.jhazmat.2014.06.058 (cit. on p. 7).

[24] M. Singh and M. Garg. "Making of anhydrite cement from waste gypsum". In: *Cement and Concrete Research* 30.4 (2000), pp. 571–577. ISSN: 0008-8846. DOI: 10.1016/S0008-8846(00)00209-X (cit. on p. 7).

[25] M. Garg, M. Singh, and R. Kumar. "Some aspects of the durability of a phosphogypsum-lime-fly ash binder". In: *Construction and Building Materials* 10.4 (1996), pp. 273–279. ISSN: 0950-0618. DOI: 10.1016/0950-0618(95)00085-2 (cit. on p. 7).

[26] Y. Min, Q. Jueshi, and P. Ying. "Activation of fly ash–lime systems using calcined phosphogypsum". In: *Construction and Building Materials* 22.5 (2008), pp. 1004–1008. ISSN: 0950-0618. DOI: 10.1016/j.conbuildmat.2006.12.005 (cit. on p. 7).

[27] T. Guo, R. F. Malone, and K. A. Rusch. "Stabilized Phosphogypsum:Class C Fly Ash:Portland Type II Cement Composites for Potential Marine Application". In: *Environmental Science & Technology* 35.19 (2001), pp. 3967–3973. DOI: 10.1021/es010520+ (cit. on p. 7).

[28] M. Taher. "Influence of thermally treated phosphogypsum on the properties of Portland slag cement". In: *Resources, Conservation and Recycling* 52.1 (2007), pp. 28–38. ISSN: 0921-3449. DOI: 10.1016/j.resconrec.2007.01.008 (cit. on p. 7).

[29] F. Akfas et al. "Geochemical and mineralogical characterization of phosphogypsum and leaching tests for the prediction of the mobility of trace elements". In: *Environmental Science and Pollution Research* 30 (15 2023-03), pp. 43778–43794. ISSN: 16147499. DOI: 10.1007/s11356-023-25357-2 (cit. on p. 7).

[30] M. S. Al-Masri et al. "Distribution of some trace metals in Syrian phosphogypsum". In: *Applied Geochemistry* 19 (5 2004-05), pp. 747–753. ISSN: 08832927. DOI: 10.1016/j.apgeochem.2003.09.014 (cit. on p. 7).

[31] H. El-Didamony et al. "Treatment of phosphogypsum waste produced from phosphate ore processing". In: *Journal of Hazardous Materials* 244-245 (2013-01), pp. 596–602. ISSN: 03043894. DOI: 10.1016/j.jhazmat.2012.10.053 (cit. on p. 7).

[32] J. Cruz. "Reações Nucleares". In: *Sebenta de Física Nuclear e das Radiações*. 2022. Chap. 10, pp. 100–108 (cit. on p. 9).

[33] J. F. Ziegler, M. Ziegler, and J. Biersack. "SRIM – The stopping and range of ions in matter (2010)". In: *Nuclear Instruments and Methods in Physics Research Section B: Beam Interactions with Materials and Atoms* 268.11 (2010), pp. 1818–1823. ISSN: 0168-583X. DOI: https://doi.org/10.1016/j.nimb.2010.02.091 (cit. on p. 11).

[34] J. Cruz. *Rutherford Backscattering Spectrometry and Elastic Backscattering Spectrometry*. Applied Nuclear Physics Lecture slides. 2022 (cit. on p. 11).

[35] J. D. Cockcroft and E. T. Walton. "Experiments with high velocity positive ions. II.-The disintegration of elements by high velocity protons". In: *Proceedings of the Royal Society of London. Series A, Containing Papers of a Mathematical and Physical Character* 137.831 (1932), pp. 229–242 (cit. on p. 14).

[36] E. Alves et al. "An insider view of the Portuguese ion beam laboratory". In: *The European Physical Journal Plus* 136.6 (2021), p. 684. DOI: 10.1140/epjp/s13360-021-01629-z (cit. on pp. 14, 17).

[37] N. P. Barradas, C. Jeynes, and R. P. Webb. "Simulated annealing analysis of Rutherford backscattering data". In: *Applied Physics Letters* 71.2 (1997-07), pp. 291–293. ISSN: 0003-6951. DOI: 10.1063/1.119524 (cit. on p. 19).

[38] A. Caciolli et al. "Proton elastic scattering and proton induced gamma-ray emission cross-sections on Na from 2 to 5MeV". In: *Nuclear Instruments and Methods in Physics Research Section B: Beam Interactions with Materials and Atoms* 266.8 (2008), pp. 1392–1396. ISSN: 0168-583X. DOI: 10.1016/j.nimb.2007.11.025 (cit. on p. 22).

[39] J. R. Vanhoy et al. "Proton resonances in ^{24}Mg from E_x=12.7 to 15.7 MeV". In: *Phys. Rev. C* 36 (3 1987), pp. 920–932. DOI: 10.1103/PhysRevC.36.920 (cit. on p. 22).

[40] V. Manteigas et al. "ERYA-Bulk and ERYA-Profiling: An application for quantitative PIGE analysis". In: *Computer Physics Communications* 275 (2022), p. 108307. ISSN: 0010-4655. DOI: 10.1016/j.cpc.2022.108307 (cit. on p. 23).

[41] J. Maxwell, W. Teesdale, and J. Campbell. "The Guelph PIXE software package II". In: *Nuclear Instruments and Methods in Physics Research Section B: Beam Interactions with Materials and Atoms* 95.3 (1995), pp. 407–421. ISSN: 0168-583X. DOI: 10.1016/0168-583X(94)00540-0 (cit. on p. 25).

[42] J. E. Salman and N. M. Hassan. "Evolution of radionuclide concentration and the radiological hazards in building material: a review". In: *Journal of Taibah University for Science* 18.1 (2024), p. 2370588. DOI: 10.1080/16583655.2024.2370588 (cit. on pp. 31, 32, 34).

[43] United Nations Scientific Committee on the Effects of Atomic Radiation. *Sources and effects of ionizing radiation. United Nations Scientific Committee on the Effects of Atomic Radiation: UNSCEAR 2000 report to the General Assembly, with scientific annexes.* Vol. 1. United Nations, 2000. ISBN: 92-1-142238-8 (cit. on pp. 31–34).

APPENDIX A

COMPLETE EBS AND PIXE DATA

Additional, supporting data is presented to complement the techniques and analysis process described throughout the main body of this dissertation. These include EBS quantification data, which was previously omitted given the higher accuracy and sensitivity of PIGE and PIXE for chemical quantification of the samples. These values can be seen in table A.1 (pp. 42, 43). It should be emphasized that EBS concentrations, although essential to enable subsequent gamma and x-ray spectra studies, are highly dependent on the used cross-section values, which come with a high degree of uncertainty, as seen in section 5.1.2 when comparing three competing sets of data. Similarly to what was mentioned for PIGE data, the NDF software, used for EBS analysis does not provide the uncertainty associated with the adjustments and, as such, the overall uncertainty of the results was impossible to calculate.

PIXE results, complete with the associated uncertainty values for a thorough understanding of the accuracy and reliability of the results, are also presented in this appendix, in tables A.2 (p. 44) and A.3 (p. 45). These were omitted from the main body to improve readability and allow for faster result interpretation.

Table A.1: Elemental composition obtained using EBS (pp. 42, 43)

Sample	Concentration (wt.%) (normalized to 100%)								
	Boron	Carbon	Nitrogen	Oxygen	Fluorine	Sodium	Magnesium	Aluminium	Silicon
L1g	7.358	0.000	0.000	62.433	8.273	1.087	1.492	2.432	0.000
Dg1	0.973	1.652	0.000	62.071	4.474	1.581	0.988	4.470	1.616
Pg1B	0.189	2.872	0.000	68.656	3.995	1.152	0.266	3.678	1.267
PgP	2.373	0.000	0.000	67.221	7.167	1.485	0.128	7.016	0.000
L3D	0.473	1.024	0.000	67.988	5.257	1.048	0.120	4.130	4.724
NRTCa	6.328	0.023	20.430	38.797	2.014	0.534	0.038	0.536	1.507
L3BS	4.046	0.000	0.000	63.862	7.874	0.519	2.098	1.955	0.000
W1DS	1.325	2.241	0.000	62.385	7.993	0.940	1.585	4.154	0.000
Na40-4-70	5.432	0.000	0.000	51.051	9.359	9.748	2.066	4.678	0.000
L1FS	6.559	0.000	0.000	59.551	7.053	3.417	0.491	3.431	0.000
W1CS	6.683	0.000	0.000	60.673	7.186	4.500	0.500	3.4957	0.000
W2BS	6.683	0.000	0.000	59.993	7.138	5.234	0.500	3.4587	0.000
NH4-RH-24	6.683	0.000	0.000	59.993	7.138	2.345	0.500	4.337	0.000
SAIS	0.000	5.862	0.000	60.760	4.052	0.240	0.002	0.044	2.720
M54	0.000	3.500	0.000	61.561	6.774	0.028	0.109	0.350	2.600
PGP	0.000	7.654	0.000	59.454	9.607	0.730	0.001	0.001	1.222
Moroccan	0.000	4-504	0.000	60.817	8.581	1.299	0.003	0.062	3.960

Sample	Concentration (wt.%) (normalized to 100%)								
	Phosphorus	Sulphur	Chlorine	Calcium	Titanium	Iron	Strontium	Cerium	Gadolinium
L1g	0.178	6.175	0.243	9.811	0.000	0.000	0.367	0.035	0.115
Dg1	0.000	14.886	0.065	6.436	0.221	0.017	0.033	0.000	0.121
Pg1B	0.000	10.214	1.947	5.311	0.029	0.000	0.230	0.002	0.192
PgP	0.000	8.252	0.019	5.819	0.052	0.000	0.277	0.023	0.168
L3D	0.000	10.342	0.009	4.450	0.008	0.000	0.251	0.015	0.161
NRTCa	0.000	10.691	11.734	6.877	0.270	0.000	0.180	0.000	0.043
L3BS	1.077	8.978	0.000	9.025	0.000	0.000	0.418	0.066	0.082
W1DS	1.226	8.224	0.000	9.319	0.000	0.001	0.329	0.588	0.221
Na40-4-70	9.087	5.757	0.631	1.851	0.014	0.000	0.197	0.000	0.126
L1FS	4.316	4.268	2.097	8.277	0.0159	0.000	0.476	0.000	0.050
W1CS	4.397	4.349	2.137	5.580	0.016	0.000	0.434	0.000	0.051
W2BS	6.089	3.998	2.137	6.234	0.072	0.000	0.476	0.000	0.051
NH4-RH-24	4.397	4.567	2.123	5.578	0.011	0.000	0.387	0.000	0.051
SAIS	0.732	8.090	8.945	2.881	0.180	0.000	0.435	0.058	0.000
M54	1.280	8.435	9.481	4.565	1.258	0.000	0.030	0.033	0.000
PGP	0.016	7.897	10.143	2.151	0.274	0.000	0.396	0.092	0.000
Moroccan	0.534	8.024	9.555	2.506	0.101	0.000	0.030	0.024	0.000

Table A.2: Elemental composition and associated fitting error percentage obtained using PIXE, with 2020 keV beam energy.

Sample	Concentration (wt.%) ± % Fitting Error (normalized to 100%)				
	Silicon	Phosphorus	Sulphur	Chlorine	Calcium
L1g	0.165 ± 192.14	0.000	23.486 ± 0.69	0.071 ± 18.45	26.997 ± 0.24
Dg1	0.611 ± 38.72	0.000	23.385 ± 0.53	0.069 ± 14.17	28.549 ± 0.20
Pg1B	0.378 ± 74.74	0.000	22.840 ± 0.71	0.067 ± 14.39	28.398 ± 0.42
PgP	0.000	0.000	23.163 ± 0.68	0.097 ± 12.91	28.022 ± 0.23
L3D	0.302 ± 112.94	0.000	23.398 ± 0.75	0.097 ± 16.87	27.406 ± 0.25
NRTCa	0.037 ± 633.05	0.000	21.946 ± 0.89	6.023 ± 0.75	27.067 ± 0.25
SAIS	0.549 ± 50.78	0.000	22.367 ± 0.64	0.076 ± 13.83	28.648 ± 0.21
M54	0.108 ± 278.97	0.194 ± 51.09	23.855 ± 0.63	0.063 ± 16.11	27.142 ± 0.20
PGP	0.339 ± 96.61	0.000	22.254 ± 0.73	0.091 ± 15.96	29.036 ± 0.23
Moroccan	0.000	6.229 ± 2.52	19.432 ± 0.65	0.046 ± 18.01	26.375 ± 0.20

Sample	Concentration (wt.%) ± % Fitting Error (normalized to 100%)				
	Titanium	Iron	Strontium	Cerium	Gadolinium
L1g	0.072 ± 3.48	0.526 ± 0.77	1.840 ± 1.86	0.112 ± 4.87	0.010 ± 50.35
Dg1	0.003 ± 29.40	0.045 ± 2.58	0.172 ± 5.39	0.000	0.008 ± 40.39
Pg1B	0.055 ± 2.28	0.034 ± 2.62	1.718 ± 1.21	0.123 ± 2.62	0.006 ± 37.57
PgP	0.060 ± 4.53	0.064 ± 2.92	1.856 ± 1.69	0.219 ± 3.06	0.022 ± 21.30
L3D	0.027 ± 8.87	0.081 ± 3.40	1.803 ± 2.66	0.091 ± 7.54	0.000
NRTCa	0.035 ± 3.88	0.047 ± 2.05	0.803 ± 1.62	0.112 ± 2.87	0.007 ± 30.25
SAIS	0.046 ± 2.83	0.067 ± 1.86	2.173 ± 1.23	0.042 ± 6.97	0.000
M54	0.012 ± 6.79	1.215 ± 0.33	0.075 ± 7.58	0.003 ± 64.94	0.000
PGP	0.086 ± 4.13	0.078 ± 2.94	2.008 ± 1.98	0.245 ± 3.39	0.012 ± 43.63
Moroccan	0.015 ± 5.22	0.095 ± 1.20	0.076 ± 6.28	0.000	0.010 ± 21.09

Table A.3: Elemental composition and associated uncertainties obtained using PIXE, with 700 keV beam energy.

Sample	Concentration (wt.%) ± % Fitting Error (normalized to 100%)					
	Sodium	Magnesium	Aluminium	Silicon	Phosphorus	Sulphur
L1g	0.129 ± 6.97	0.000	0.036 ± 8.61	0.233 ± 2.37	0.239 ± 3.41	23.115 ± 0.11
Dg1	0.045 ± 20.37	0.564 ± 1.11	0.144 ± 2.78	0.710 ± 0.69	0.000	22.362 ± 0.09
Pg1B	0.050 ± 19.39	0.007 ± 74.26	0.058 ± 6.79	0.470 ± 1.37	0.171 ± 4.94	21.451 ± 0.11
PgP	0.069 ± 13.91	0.013 ± 36.05	0.089 ± 4.18	0.322 ± 1.97	0.267 ± 3.37	22.790 ± 0.12
L3D	0.025 ± 34.09	0.002 ± 253.87	0.013 ± 24.29	0.422 ± 1.42	0.174 ± 4.72	22.980 ± 0.11
NRTCa	0.053 ± 23.25	0.001 ± 429.84	0.030 ± 14.48	0.546 ± 1.37	0.078 ± 12.54	21.685 ± 0.22
SAIS	0.039 ± 12.77	0.004 ± 58.11	0.030 ± 6.34	0.444 ± 0.84	0.079 ± 6.09	22.975 ± 0.16
M54	0.132 ± 5.60	0.031 ± 11.12	0.045 ± 5.63	0.434 ± 0.88	1.364 ± 0.57	23.614 ± 0.08
PGP	0.063 ± 6.12	0.010 ± 19.90	0.135 ± 1.25	1.138 ± 0.30	0.276 ± 1.40	22.235 ± 0.12
Moroccan	0.358 ± 2.86	0.455 ± 1.30	0.123 ± 2.77	0.255 ± 1.72	7.238 ± 0.20	18.544 ± 0.12

Sample	Concentration (wt.%) ± % Fitting Error (normalized to 100%)					
	Chlorine	Calcium	Titanium	Iron	Strontium	Cerium
L1g	0.067 ± 7.74	26.772 ± 0.19	0.061 ± 11.5	0.594 ± 3.92	2.022 ± 0.73	0.183 ± 11.14
Dg1	0.085 ± 8.33	29.207 ± 0.16	0.000	0.090 ± 34.39	0.237 ± 4.87	0.030 ± 144.1
Pg1B	0.069 ± 12.29	29.714 ± 0.18	0.053 ± 34.83	0.132 ± 35.69	2.099 ± 0.79	0.166 ± 38.00
PgP	0.080 ± 7.03	27.497 ± 0.21	0.045 ± 18.69	0.103 ± 12.61	2.089 ± 0.81	0.241 ± 11.31
L3D	0.067 ± 7.73	27.408 ± 0.19	0.020 ± 29.98	0.048 ± 18.99	2.200 ± 0.73	0.108 ± 15.94
NRTCa	5.121 ± 0.52	26.304 ± 0.36	0.035 ± 23.88	0.119 ± 14.64	1.002 ± 1.89	0.105 ± 26.23
SAIS	0.066 ± 4.73	27.267 ± 0.20	0.066 ± 6.57	0.021 ± 21.97	2.526 ± 0.41	0.039 ± 23.94
M54	0.057 ± 7.43	24.164 ± 0.16	0.014 ± 36.38	2.105 ± 1.49	0.059 ± 16.76	0.000
PGP	0.065 ± 3.50	27.283 ± 0.15	0.078 ± 4.92	0.076 ± 6.32	1.950 ± 0.43	0.244 ± 4.66
Moroccan	0.051 ± 8.64	24.893 ± 0.18	0.012 ± 44.34	0.074 ± 13.90	0.086 ± 13.66	0.000